

1 **Precipitation Enhancement in Squall Lines Moving Over Mountainous Coastal Regions**



2
3 Fan Wu and Kelly Lombardo

4
5 Department of Meteorology and Atmospheric Science, The Pennsylvania State University,
6 University Park, Pennsylvania, USA

7
8 Submitted to *Journal of the Atmospheric Sciences*

9 in July 2020

10 Revised in January 2021

11 Revised in April 2021

12 Revised in June 2021

13
14
15
16
17
18
19
20
21
22

Corresponding author: Fan Wu, fvw5116@psu.edu

Early Online Release: This preliminary version has been accepted for publication in *Journal of the Atmospheric Sciences*, may be fully cited, and has been assigned DOI 10.1175/JAS-D-20-0222.1. The final typeset copyedited article will replace the EOR at the above DOI when it is published.

23
24
25
26
27
28
29
30
31
32
33
34
35
36
37
38
39
40
41
42
43
44
45

ABSTRACT

A mechanism for precipitation enhancement in squall lines moving over mountainous coastal regions is quantified through idealized numerical simulations. Storm intensity and precipitation peak over the sloping terrain as storms descend from an elevated plateau toward the coastline and encounter the marine atmospheric boundary layer (MABL). Storms are most intense as they encounter the deepest MABLs. As the descending storm outflow collides with a moving MABL (sea breeze), surface and low-level air parcels initially accelerate upward, though their ultimate trajectory is governed by the magnitude of the negative non-hydrostatic inertial pressure perturbation behind the cold pool leading edge. For shallow MABLs, the baroclinic gradient across the gust front generates large horizontal vorticity, a low-level negative pressure perturbation, and thus a downward acceleration of air parcels following their initial ascent. A deep MABL reduces the baroclinically-generated vorticity, leading to a weaker pressure perturbation and minimal downward acceleration, allowing air to accelerate into a storm's updraft.

Once storms move away from the terrain base and over the full depth of the MABLs, storms over the deepest MABLs decay most rapidly, while those over the shallowest MABLs initially intensify. Though elevated ascent exists above all MABLs, the deepest MABLs substantially reduce the depth of the high- θ_e layer above the MABLs and limit instability. This relationship is insensitive to MABL temperature, even though surface-based ascent is present for the less cold MABLs, the MABL thermal deficit is smaller, and convective available potential energy (CAPE) is higher.

46 **1. Introduction**

47 Precipitation enhancement is frequently observed over coastal regions (Ogino et al. 2016;
48 Curtis 2019), with distinguishable spatial maxima centered on and surrounding coastlines.
49 Tropical Rainfall Measuring Mission (TRMM) precipitation data show that precipitation amounts
50 peak along coastlines and decrease rapidly within 300 km of the land-sea boundary (Ogino et al.
51 2016). Long-term (1931–2010) Global Precipitation Climatology Center (GPCC) V2018
52 reanalysis confirm these localized coastal maxima and reveal that their magnitudes have increased
53 in recent decades, impacting coastal residents, offshore recreational and commercial activities, and
54 coastal ecosystems (Curtis 2019). Physical mechanisms responsible for the precipitation
55 enhancement are related to land-sea interactions (e.g., sea breeze), with 40–60% of total rainfall
56 over the Mediterranean and Maritime Continent associated with coastal circulations, for example
57 (Bergemann et al. 2015). An important source of coastal precipitation is seaward propagating
58 mesoscale convection system (MCS), or squall lines, which are modified by these coastal
59 circulations (Wu et al. 2009; Lombardo and Colle 2011, 2012, 2013; Li and Carbone 2015;
60 Lombardo and Kading 2018, hereafter LK18). Therefore, advancing our knowledge of the
61 mechanisms responsible for coastal precipitation enhancements necessitates an understanding of
62 deep convective storm dynamics over coastal environments.

63 As deep convective storms move from inland to offshore, precipitation is dictated by
64 characteristics of a storm’s cold pool and the ambient stable marine atmospheric boundary layer
65 (MABL) air driving a local sea breeze (Moncrieff and Liu 1999; Zuidema et al. 2017; LK18).
66 Given the importance of cold pools in the offshore movement of coastal storms (de Szoeke et al.
67 2017), it is instructional to revisit the associated fundamental convective initiation (CI)
68 mechanisms before considering modifications induced by the MABL. One of the leading theories

69 on squall line dynamics poses that squall-line strength and longevity are influenced by horizontal
70 vorticity baroclinically generated by the cold pool and that of the ambient low-level wind shear,
71 known as “RKW theory” (Rotunno et al. 1988; Moncrieff and Liu 1999; Tompkins 2001; Weisman
72 and Rotunno 2004; Bryan and Rotunno 2014; Torri et al. 2015). Based on this theory, the vertical
73 orientation of lifting at the cold pool leading edge (CPL) can be determined by the ratio of cold
74 pool intensity (C) to ambient low-level wind shear (Δu), or $C/\Delta u$ [see Fig. 2 in Weisman and
75 Rotunno (2004)]. The frontal lifting is downshear (upshear) tilted when $C < \Delta u$ ($C > \Delta u$), or
76 optimally upright when a balance is achieved ($C = \Delta u$).

77 Moving density currents, such as cold pool outflows and sea breezes, are associated with
78 increased low-level vertical wind shear and can alter this balance. The associated increase in low-
79 level mass convergence can also promote CI (e.g., Droegemeier and Wilhelmson 1985; Wilson
80 and Schreiber 1986; Carbone et al. 1990; Kingsmill 1995; Moncrieff and Liu 1999; Banacos and
81 Schultz 2005), though not always. A deep convective storm over coastal Queensland Australia
82 during the Coastal Convective Interactions Experiment (CCIE) was anticipated to intensify as it
83 moved into the marine environment through deeper cold-pool-lifting by the increased low-level
84 vertical wind shear, though the storms dissipated (Soderholm et al. 2016). Dissipation was
85 hypothesized to result from the elevated level of free convection (LFC) in the marine environment,
86 though differences in density between the outflow and MABL may have played a role as well. The
87 vertical slope at the interface of the two moving fluids is sensitive to their buoyancies, tilting
88 toward the denser fluid (van der Wiel et al. 2017; Cafaro and Rooney 2018), thus impacting an air
89 parcel’s vertical trajectory, CI, and precipitation.

90 Storm dynamics are also influenced by the marine environment following the initial
91 engagement with the MABL. Perhaps counterintuitively, sea surface temperature (SST) is not a

92 good predictor for MCS longevity over the coastal waters (Lombardo and Colle 2012). Rather, the
93 presence of strong environmental 0–3-km wind shear is critical, and can help sustain storms >100
94 km offshore (Lombardo and Colle 2012). Contrasting case studies of northeastern U.S. quasi-linear
95 convective systems (QLCSs) showed that bores can form following the collision between a
96 QLCS’s cold pool and a MABL, which can successfully move storms over the stable layer
97 (Lombardo and Colle 2013). Here, enhanced low-level vertical wind shear helps trap the wave
98 energy within the boundary layer maintaining the bore (LK18), rather than provide a source of
99 horizontal vorticity. Further, the reduced buoyancy gradient across the cold pool-MABL interface
100 limits the baroclinic development of vorticity. Rather, pre-collision cold pool-MABL buoyancy
101 differences determine bore development, with bores forming when the MABL is denser than the
102 cold pool (LK18). Though bores provided a mechanism to successfully move storms over the
103 coastal waters, conditions in the free troposphere determine storm intensity and precipitation
104 (LK18; Lombardo 2020).

105 To add further complexity, squall lines often occur over coastal regions with orography
106 along or immediately upstream of the coastline (Kömüşçü et al. 1998; Teng et al. 2000; Mapes et
107 al. 2003; Warner et al. 2003; Cohuet et al. 2011; Pucillo et al. 2019), influencing CI and preexisting
108 convection. Prior studies have primarily focused on the impact of inland orography on squall line
109 evolution, specifically a storm’s ability to successfully traverse a mountain range (Frame and
110 Markowski 2006; Reeves and Lin 2007; Letkewicz and Parker 2010, 2011; Smith et al. 2014).
111 Terrain-crossing squall lines often propagate discretely, leading to heterogeneous precipitation
112 patterns across the ridge (Teng et al. 2000; Frame and Markowski 2006). Storms initially intensify
113 through orographic lift as they ascend a mountain, but weaken in the lee slope as their cold pools
114 become partially blocked by the terrain. Gravitational descent down the lee slope further thins and

115 warms the cold pools, limiting their ability to lift parcels to their LFCs, resulting in a precipitation
116 shadow. Storms can ultimately re-intensify at the terrain base if the flow transitions from
117 supercritical to subcritical, supporting intense vertical motion (Frame and Markowski 2006). The
118 environment in the lee also influences ridge-crossing, with success favored in the presence of
119 comparatively high lee-side instability, though mean wind plays an increasingly important role
120 when convective available potential energy (CAPE) is substantially reduced (Letkewicz and
121 Parker 2010, 2011), such as in the marine environment.

122 To the authors' knowledge, only a limited number of studies have examined deep
123 convective storm evolution over mountainous coastal regions. Daytime onshore sea breezes over
124 coastal Columbia were shown to modify coastal precipitation development and propagation as
125 they ascend the coastal terrain as upslope flows (López and Howell 1967; Warner et al. 2003).
126 Gravity waves were also shown to support the offshore propagation of organized convection over
127 western South America, though the waves formed from diurnal variations in elevated heating over
128 the coastal mountain peak rather than through cold pool-MABL interactions (Mapes et al. 2003).
129 Systematic quantification of coastal squall line dynamics, specifically the impact of elevated
130 topography and onshore sea breeze flows, is absent in the literature. Given the globally ubiquitous
131 nature of squall lines over mountainous coastal regions, and the impact of these environmental
132 features on heavy, convective precipitation, it is prudent to identify the physical processes
133 controlling storm evolution. Advancements in our understanding of the fundamental dynamics
134 may improve prediction of these hazardous storms. Toward this end, idealized numerical
135 experiments are designed to quantify the modification to storm dynamics by a mountain and
136 moving MABLs. Section 2 describes these experiments, as well as the base-state, terrain, and
137 MABL characteristics. Methods to identify the CPLE and to diagnose components of the vertical

138 acceleration are introduced as well. Section 3 describes storm evolution in the constructed coastal
139 environment, and the dynamics of enhanced precipitation over the terrain slope is presented in
140 Section 4. Storm evolution once over the MABL is presented in Section 5, with discussions and
141 conclusions in Sections 6 and 7, respectively.

142 **2. Methods**

143 *a. Model configuration*

144 Large-eddy simulations are performed with the Cloud Model 1 (CM1) version 19, a non-
145 hydrostatic, cloud-resolving numerical model (Bryan and Fritsch 2002). The 800-km (horizontal)
146 \times 20-km (vertical) two-dimension domain is sufficiently large to limit the influence of the lateral
147 boundaries on storm evolution. The horizontal domain has 200-m grid spacing, and the vertical
148 resolution is stretched from 50-m below 3 km to 250-m above 10 km. A terrain-following
149 coordinate system is used, following Gal-Chen and Somerville (1975). The horizontal boundaries
150 are open-radiative, with free-slip conditions at the top and bottom boundaries. Numerical
151 parameterizations used to estimate physical processes include the Morrison double-moment
152 microphysical scheme (Morrison et al. 2009), which includes predictions of cloud droplets, cloud
153 ice, rain, snow, and graupel, and a TKE subgrid-scale turbulence scheme (Deardorff 1980). No
154 radiation and surface fluxes are included to eliminate the influence of time-varying parameters
155 (i.e., diurnal cycle) and isolate the influence of the MABL and orography on storms. The model is
156 integrated for 480 min using a Runge-Kutta scheme, with a large time step of 0.75 s. Other model
157 configurations follow LK18.

158 *b. Orography*

159 Plateau-shaped terrain is included as a simplified representation of the coastal terrain
160 structure in regions that experience coastal squall lines, such as the eastern U.S., China, the

161 Mediterranean, and South America. A 1.5-km plateau is included from 0–300 km, with a slope
162 extending from the plateau top to the base (300–360 km), with values based on commonly
163 observed coastal orography in squall-line-active regions. A storm moving over this terrain in the
164 absence of a MABL is used as a reference (“CTRL”) for comparison to additional terrain
165 experiments, and to simulations which include a MABL at the terrain base (see Section 3a). Initial
166 experiments quantify the plateau’s influence on storm evolution, by removing the feature
167 (“NoTER”) and extending the elevated surface across the full domain (“OnlyTER”). The bulk of
168 the experiments quantify storm response as they descend the plateau and collide with a moving
169 MABL, with depths of 500 m, 1000 m, and 1500 m and potential temperature perturbations (θ') of
170 -2 K, -3 K, -4 K, and -5 K relative to the base-state. MABL values are informed by observations
171 and prior work (Lombardo and Colle 2013; LK18; Lombardo 2020).

172 *c. Base-state environment*

173 Simulations are initialized with a horizontally homogeneous base-state environment by
174 using an analytic thermodynamic profile, informed by observed soundings during coastal squall
175 line events (Fig. 1a; Lombardo 2020). Vertical wind shear is 15 m s^{-1} in the lowest 3.5 km. For
176 regions with terrain, the profile below the surface is truncated by the model to maintain the
177 horizontally homogeneous initial conditions, which is commonly used in idealized simulations of
178 squall lines over mountainous regions (Frame and Markowski 2006; Letkewicz and Parker 2011;
179 Reeves and Lin 2007). In this way, the initial conditions inhibit artificial convection caused by a
180 horizontally heterogeneous base-state environment. With the lower part of the profile removed
181 below the terrain surface, base-state environmental variables over the mountainous region vary
182 and deviate from those at ‘sea level’. For example, surface-based convective available potential
183 energy (SBCAPE) and most-unstable convective available potential energy (MUCAPE) are

184 738.69 J kg⁻¹ and 917.50 J kg⁻¹ over the plateau top, respectively, but 1596.95 J kg⁻¹ and 1630.53
185 J kg⁻¹ at the bottom. Additional base-state thermodynamic parameters are provided in Table 1.
186 Base-state wind shear also decreases from 15 m s⁻¹ at the plateau base to 9 m s⁻¹ at the top.
187 Although the instability is diminished on the plateau top, it is able to support a mature squall line.

188 *d. Storm and MABL initiation*

189 Storms are initiated at $t = 0$ on the plateau top through momentum forcing (Morrison et al.
190 2015), with 20-km wide convergence centered 200 km from the left boundary, which decreases
191 from the ground to 10 km above ground level (AGL).¹ A 0.2 m s⁻² magnitude forcing is applied
192 from 0–55 min, which ramps down from 55–60 min. Storms reach maturity before encountering
193 the plateau edge. The MABL is inserted at $t = 0$ as a block of relatively dense air (LK18; Lombardo
194 2020), from the base of the plateau to the domain edge (360–800 km). This allows the MABL to
195 move toward the sloping terrain as a sea breeze. Water vapor mixing ratio within the MABL is
196 held constant, resulting in a cloud layer for cooler, deeper MABLs. The MABL is not continuously
197 forced, which leads to a sloped leading edge as it moves toward and ascends the slope. The
198 inclusion of a MABL reduces the instability at the base of terrain by providing a stably stratified
199 surface-based layer, with properties governed by the MABL depth and θ' (Fig. 1b, Table 2).

200 *e. Identification of CPLE*

201 The CPLE is identified, tracked, and used as a point of reference for evaluating the evolving
202 storm physical processes. Previous studies have used various methods to identify the CPLE, such
203 as a rapid drop in temperature (de Szoeke et al. 2017), the largest horizontal gradient of potential
204 temperature (θ) at the lowest model level (Grant and van den Heever 2016), or the specific negative
205 buoyancy contour (e.g., $-0.005 \text{ m}^2 \text{ s}^{-1}$; Tompkins 2001; Feng et al. 2015). For this study, CPLE

¹ Sensitivity to storm initiation location was tested (centered 100 km, 150 km) with similar results.

206 identification using these methods becomes challenging once storms encounter a MABL, due to a
207 reduction in the horizontal temperature gradient across the cold pool-MABL interface. Therefore,
208 the CPLE is identified as the largest horizontal gradient of equivalent potential temperature (θ_e) at
209 the lowest model level (25 m AGL). This method exploits the pronounced moisture gradient across
210 the cold pool-MABL interface. Dissipation of the CPLE occurs once the θ_e gradient falls below 1
211 $\times 10^{-3} \text{ K m}^{-1}$. Different threshold values within this range (e.g., 2×10^{-3} and $5 \times 10^{-3} \text{ K m}^{-1}$) have
212 been tested with minimal differences.

213 *f. Decomposition of vertical accelerations and pressure perturbations*

214 A number of studies have decomposed vertical accelerations and pressure perturbations to
215 diagnose the physical processes dominating storm evolution (Jeevanjee and Romps 2015, hereafter
216 JR15; Dawson et al. 2016; Peters 2016; Schenkman et al. 2016; LK18; Huang et al. 2019). Here,
217 similar analyses are derived, though from the anelastic momentum equation in perturbation form,
218 rather than from the full equation (e.g., JR15). Unique to this study, the nonhydrostatic pressure
219 perturbation (p'_{nh}) is decomposed into buoyant [$p'_{b(nh)}$] and inertial [$p'_{i(nh)}$] components. Sources of
220 $p'_{i(nh)}$ are further partitioned into contributions from the *splat* (deformation) and *spin* (vorticity)
221 terms. Vertical acceleration is decomposed into buoyant (a_b) and inertial (a_i) accelerations, with
222 the full derivations in the Appendix.

223 **3. Storm evolution**

224 *a. Impact of terrain only*

225 To quantify the effects of plateau-shaped terrain on squall line evolution, we first varied
226 the terrain configuration (“CTRL”, “NoTER”, “OnlyTER”) in the absence of a MABL. Following
227 initiation, the CTRL squall line matures by 60 min, prior to reaching the plateau top eastern edge
228 (300 km), with precipitation mixing ratio plumes exceeding 12 km in altitude (Fig. 2a1):

229 Hydrometeor mass is used as a measure of storm intensity. By 120 min, the storm begins its descent
230 downslope and weakens, expressed by a reduced precipitation mixing ratio (Fig. 2a2). Once at the
231 plateau base, the storm re-intensifies (180 min; Fig. 2a3) and remains robust through 240 min (Fig.
232 2a4) to the end of the simulation (not shown). A Hovmöller diagram of total column precipitation
233 mass emphasizes the reduction in precipitation over the sloping terrain (e.g., Frame and
234 Markowski 2006), with a substantial decrease from the plateau edge (300 km) to just west of the
235 plateau base (360 km; Fig. 3a).

236 Without terrain (“NoTER”), the squall line is more intense during the initial two hours
237 (Figs. 2b1–2, 3b), in part due to the larger environmental instability and low-level vertical wind
238 shear than over the plateau top (Table 1). The storm weakens over the following several hours,
239 though the smaller precipitation mass between 300–360 km is associated with natural storm
240 evolution following initiation rather than terrain (Figs. 2b3–4, 3b). By 420 min, the squall line is
241 almost fully decayed (Fig. 3b), showing that the presence of a plateau extends the lifetime of the
242 storm.

243 For a continuously elevated 1.5-km surface (“OnlyTER”), the storm’s initial evolution is
244 very similar to the CTRL storm (Figs. 2c1–2, 3c). After 120 min, it is weaker and shallower than
245 in the other experiments (Figs. 2c3–4, 3c), with a similar decay time to the NoTER storm (Figs.
246 3b,c). Therefore, the re-intensification of the CTRL storm is in response to the sloping terrain,
247 which will be discussed in Sections 4 and 5.

248 *b. Precipitation evolution with a MABL*

249 A squall line’s precipitation is modified as it descends the plateau slope and encounters the
250 MABL, though the precipitation trends differ while a storm is over the slope versus at the plateau
251 base (Fig. 4). Therefore, analyses are presented in three phases: when the storm is (1) over the

252 plateau top (0–90 min), (2) over the slope (90–150 min), and (3) at the base (150–480 min). Over
253 the plateau top, the magnitude and structure of the precipitation mass are essentially the same
254 among the experiments. Over the slope, precipitation mass diverges as a function of MABL depth
255 and θ' . Generally, precipitation is largest for the storm encountering the deepest MABL and
256 declines with decreasing MABL depth. Such precipitation differences are associated with
257 differences in storm intensity, highlighted by temporally-zoomed-in timeseries of maximum
258 vertical velocity (w_{\max}), total precipitation mass, and rain rate (Fig. 5; Cecil and Zipser 1999; Xu
259 and Wang 2015; Grant and van den Heever 2016). As storms initially collide with the upslope
260 moving MABL, w_{\max} increases from 3–4 m s^{-1} to 13–18 m s^{-1} , with the largest and earliest w_{\max}
261 increases for storms encountering the deepest MABLs (Fig. 5a). For the CTRL storm, the collision
262 with the ambient upslope flow in the absence of a MABL generates the weakest w_{\max} . Total
263 precipitation mass and rain rate (magnitude and timing) respond to this change in vertical motion,
264 with the most intense and earliest precipitation enhancements during storm interactions with the
265 deepest MABLs (Figs. 5b,c). The relationship between precipitation mass and MABL θ' is less
266 clear, though precipitation is initially largest in the experiment with deepest and coldest (1500-m
267 deep, $-5\text{-K } \theta'$) MABL. Details of and dynamics associated with this precipitation peak are
268 presented in Section 4.

269 Once the squall lines reach the base and move away from the slope (after 150 min), the
270 trend of precipitation mass with MABL depth reverses, with values generally continuing to
271 increase until 240 min for storms over the shallowest MABLs, and declining for storms over the
272 deepest MABLs (Fig. 4). While no robust relationship exists between MABL θ' and storm
273 precipitation, more precipitation mass is produced for storms over the least cold ($-2\text{-K-}\theta'$) 500-m
274 and 1500-m deep MABLs. Further, the impacts of MABL θ' are more obvious for storms over the

275 deepest MABL; Precipitation mass decreases more quickly while over the $-5\text{-K-}\theta'$ MABL than
276 the $-2\text{-K-}\theta'$ MABL.

277 *c. Storm-scale evolution over terrain with no MABL*

278 Transitions in precipitation trends are presented in detail for the CTRL and a subset of
279 representative MABL experiments, $-5\text{-K-}\theta'$ for all depths, with consistent processes and trends for
280 storms over the less cold (-2-K , -3-K , -4-K θ') MABLs. Cross sections of mixing ratio (q),
281 equivalent potential temperature (θ_e), and buoyancy (B) provide insight into structural changes for
282 individual storms. For the CTRL storm interacting with the upslope ambient flow (Fig. 6a), the
283 leading line convective plumes become shallower as the squall line descends down the slope (120
284 min; Fig. 7a1). As the cold pool moves downslope, its depth decreases (< 1 km) and the associated
285 B increases (Fig. 7c1; e.g., Frame and Markowski 2006), resulting in a decline of cold pool speed
286 from 13.03 m s^{-1} on the plateau top (90–100 min) to 5.43 m s^{-1} on the slope (120–130 min).² This
287 thinning and warming reduce the cold pool-driven lifting, contributing to relatively shallow
288 (ground–4 km) vertical motion (Fig. 7c1). Though air parcels rise to their lifting condensation
289 levels (LCLs; Fig. 7b1) and LFCs (0.99 km AGL), the updraft core, defined loosely as a plume of
290 relatively high θ_e , is comparatively thin while over the slope (Fig. 7b1), with lower θ_e values than
291 the boundary layer source region, resulting in the smallest precipitation (Fig. 7a1).

292 At the plateau base (180 min), the storm intensifies (Fig. 7a2) as the cold pool deepens to $>$
293 2 km (Figs. 7b2,c2), more effectively lifting surface parcels to their LFC in the presence of 1597
294 J kg^{-1} of SBCAPE (Table 1). The associated vertical motion is tropospheric-deep, drawing high-
295 θ_e boundary layer air into the storm (Fig. 7b2), leading to greater precipitation (Fig. 7a2). The
296 squall line remains well-organized and continues across the domain through 300 min (Figs. 7a3–

² The calculations of cold pool speed follow the method in Grant and van den Heever (2016).

297 c3).

298 *d. Storm-scale evolution over terrain including a MABL*

299 Squall line vertical motion depth and magnitude are enhanced over the slope as storms
300 collide with the advancing MABLs (Figs. 6b–d), with CI favored for progressively deeper MABLs
301 (Figs. 8–10). The collision between a storm’s cold pool and the deepest MABL (Fig. 6d) initiates
302 an intense ($q > 7 \text{ g kg}^{-1}$), deep ($> 7 \text{ km}$) convective plume (Fig. 8a1) and deep ascent (Figs. 8b1,c1),
303 contributing to a substantial increase in precipitation (Fig. 4). Despite the overall reduction in low-
304 level potential instability in the downstream marine environment, relatively undiluted, high- θ_e air
305 from above the MABL is transported into the updraft (Fig. 8b1). Low-CAPE (455.22 J kg^{-1}),
306 negatively buoyant ($-5.96 \times 10^{-2} \text{ m s}^{-2}$) MABL air is mechanically lifted into the storm as well,
307 with 10-min average mean vertical displacement (z_{10}) of 3.71 km (Table 3). The more buoyant air
308 ($\geq -0.07 \text{ m s}^{-2}$) near the MABL top rises unhindered ($> 6 \text{ km}$; Fig. 11c), while the least buoyant
309 air ($< -0.10 \text{ m s}^{-2}$) achieves smaller vertical excursions and descends after the initial lift (Fig. 11c).

310 Once at the plateau base, the squall begins to decay (Figs. 8a2–c2,a3–c3). Compared with
311 the CTRL, the cold pool experiences a similar deepening and strengthening at the plateau bottom,
312 but the MABL reduces the boundary-layer- θ_e , decreasing the low-level horizontal buoyancy
313 gradient (Table 3). Consequently, updrafts become elevated above the surface (Fig. 8c2).
314 Negatively buoyant air from the upper-marine layer rises into the storm along sloped trajectories
315 (Table 4), while the least buoyant parcels descend into the westward MABL flow (Fig. 11f),
316 illustrating that the cold pool outflow and surface-base lifting has weakened. Relatively rapidly,
317 the updraft slows, contracts, and begins to tilt downshear (Figs. 8b2–c2,b3–c3), contributing to a
318 loss of precipitation (Figs. 8a2,a3).

319 Collision with a moderately deep (1000-m) MABL (Fig. 6c) yields smaller, shallower

320 mixing ratios (Fig. 9a1), lower θ_e (Fig. 9b1), and smaller vertical motion (Fig. 9c1) within the
321 convective plumes. Average vertical velocity of MABL air is lower (Table 3), with updrafts ≥ 4 m
322 s^{-1} (≥ 12 m s^{-1}) restricted to below 5 km (3 km; Fig. 9c1). Despite their larger CAPE (705.38 J
323 kg^{-1}), MABL parcels descend after rising only 2–3.5 km, with the exception of the most buoyant
324 MABL parcels which ascend to 5 km (Fig. 11b; Table 3). Once at sea level, even the least buoyant
325 marine air parcels ascend into the updrafts, with larger vertical displacements, velocities, and
326 CAPE than in the deepest MABL experiment (c.f., Figs. 11e,f; Table 4). The MABL reduces the
327 available potential instability, however, and by 300 min, only weak elevated, weak convection
328 remains (Figs. 9a3–c3).

329 Collision with the shallowest (500-m) MABL (Fig. 6b) produces even less convective
330 precipitation (Fig. 10a1), though low-level θ_e (Fig. 10b1) and vertical motion (Fig. 10c1) are larger
331 than for the prior experiment. Parcels ascend more slowly along sloped trajectories with smaller
332 average vertical displacements (Fig. 11a; Table 3), regardless of their larger CAPE (1052.54 J kg^{-1});
333 After rising 2–3 km, they all descend toward the surface (Fig. 11a). Once away from the terrain,
334 intensity of the now elevated storm is similar to the CTRL (Figs. 10a2–c2), though the least
335 buoyant MABL air remains below 1 km (Fig. 11d). Unlike the CTRL, there are signs of weakening
336 as the storm traverses the domain. The high- θ_e conduit is no longer tropospheric-deep (Fig. 10b3),
337 with evidence of a downshear tilt.

338 **4. Mechanism for the precipitation enhancement over the slope**

339 Pressure perturbation and vertical acceleration analyses provide additional insight into the
340 observed precipitation enhancement for storms over mountainous coastal regions, and the
341 associated ascent characteristics after the initial collision between cold pool and upslope flow.

342 *a. Storm-scale physical processes over terrain with no MABL*

343 Collision of the cold pool and upslope flow (no MABL) yields positive total vertical
344 acceleration (dw/dt) around the CPLE from the surface–2 km, dominated by inertial processes ($a_i >$
345 $8 \times 10^{-2} \text{ m s}^{-2}$; Fig. 12a), suggesting that cold-pool-driven lifting is the major process responsible
346 for the low-level ascent. The smaller buoyant acceleration ($a_b < 2 \times 10^{-2} \text{ m s}^{-2}$) also contributes
347 positively to the lifting of high- θ_e ambient layer ahead of (i.e., east of) the CPLE, with negative
348 acceleration behind (i.e., west of) the CPLE (Fig. 12a). Following the initial lift, parcel ascent
349 above 2 km is inhibited by a negative dw/dt center (primarily $a_i < -6 \times 10^{-2} \text{ m s}^{-2}$) displaced above
350 the cold pool behind the CPLE (Fig. 12a). The force driving these accelerations is primarily the
351 nonhydrostatic component of the perturbation pressure gradient force (NPPGF; Fig. 12b). Positive
352 inertial acceleration at the CPLE is due to an upward inertial NPPGF associated with a near-surface
353 $p'_{i(nh)}$ maxima. Negative inertial acceleration west of the CPLE is caused by a downward NPPGF
354 associated with a low-level $p'_{i(nh)}$ minima (Figs. 12b,c). This negative NPPGF limits the vertical
355 displacement of the CTRL air parcels after their initial lift, limiting the generation of precipitation.

356 More in-depth physical understanding of these pressure perturbations, which are critical in
357 determining the fate of the air parcels, can be revealed by decomposing the $p'_{i(nh)}$ field into its
358 individual contributing processes, which include the convergence/deformation of the wind field
359 (“*splat*” term, positive contribution) and the rotation of the wind field (“*spin*” term, negative
360 contribution; see Appendix for details). Physically, positive $p'_{i(nh)}$ is associated with convergence
361 (*splat*) around the CPLE (Fig. 12d) as the cold pool encounters the upslope flow. Negative $p'_{i(nh)}$
362 behind the CPLE is associated with horizontal vorticity (*spin*; Fig. 12d), generated baroclinically
363 due to horizontal gradients of buoyancy ($-\partial B/\partial x$; Figs. 12e,f; Trapp and Weisman 2003; Xu et al.
364 2015; Markowski 2016). The associated vorticity minimum is displaced slightly behind the
365 baroclinic generation ($-\partial B/\partial x$) minimum due to rearward advection following its development

366 (Fig. 12f). These physical processes explain the shallow updraft and the small precipitation
367 enhancement over the slope. The near-surface positive $p'_{i(nh)}$ associated with the cold pool-upslope
368 flow convergence accelerates parcels upward. The elevated negative $p'_{i(nh)}$ associated with
369 baroclinically-generated horizontal vorticity due to the sharp B gradient across the cold pool
370 interface then accelerates parcels downward, suppressing updraft development.

371 *b. Storm-scale physical processes over terrain including a MABL*

372 The magnitudes and locations of these vertical accelerations and nonhydrostatic pressure
373 perturbations are altered by the upslope moving MABL. Generally, the near-surface positive total
374 vertical accelerations at the CPLE (dw/dt^+) and the associated positive $p'_{i(nh)}$ are similar to those
375 for the CTRL storm, with minimal differences in their locations and magnitudes (Table 5; Fig. 13).
376 The most notable differences are for the storm colliding with the deepest MABL, with 15–20%
377 larger total acceleration ($4.09 \times 10^{-2} \text{ m s}^{-2}$), owing to 15–20% greater convergence at the CPLE
378 (Table 5; Fig. 13g), due to the deeper, stronger upslope flow (Fig. 6d). Considering parcel motion
379 above this initial cold pool lift, the most critical differences lay behind the CPLE, in the negative
380 dw/dt above the cold pool (dw/dt^-). The presence of the MABL decreases the horizontal buoyancy
381 gradient between cold pool and adjacent ambient atmosphere, which reduces the baroclinically-
382 generated horizontal vorticity (Figs. 13c,f,i), the associated negative $p'_{i(nh)}$ (Figs. 13b,e,h), and the
383 downward inertial acceleration (Figs. 13a,d,g; Table 5). As a result, the magnitude of the
384 downward total vertical acceleration is reduced and its center is displaced upward, allowing for
385 deeper and stronger ascending motion, and subsequently more precipitation. MABL depth
386 determines the reduction in magnitude and increase in height of these minima, with weaker and
387 more elevated minima for deeper MABLs (Figs. 13a,d,g).

388 **5. Processes governing storm evolution at the plateau base**

389 Arrival at the plateau base allows the CTRL storm and those encountering the shallowest
390 MABLs to re-intensify, while those moving over the deeper MABLs begin to decay. Analyses
391 range from 150–170 min, beginning once the storms reach the plateau base (Figs. 7–10). With no
392 MABL, the storm’s cold pool deepens and yields larger ascent at a new CPLE (denoted by “A” in
393 Fig. 14b1) that forms ~4 km downstream of the original boundary (denoted by “B” in Fig. 14b1),
394 that now exhibits vertically stacked positive and negative centers limiting ascent (Figs. 14a1–c1).
395 As the storm moves across the bottom, positive acceleration around the new CPLE deepens and
396 intensifies, with buoyant processes initially playing a more dominant role (Figs. 14b2,c3).
397 Consequently, surface-based high- θ_e air is lifted to the LFC (~1 km; Figs. 14a2,a3) and moisture
398 is fluxed vertically, promoting CI and precipitation (Figs. 14c2,c3). However, elevated negative
399 acceleration is still present behind the CPLE, contributing to sloped and weaker ascent (Figs. 14c2).

400 In contrast, advancement over the deepest MABL results in essentially the elimination of
401 the horizontal buoyancy gradient across the CPLE, and the lowest levels are ultimately dominated
402 by the westward moving MABL (Fig. 15a1). Positive vertical acceleration at the CPLE weakens
403 as the near-surface convergence dissipates, and is replaced by downward buoyant acceleration (a_b)
404 from the negatively buoyant MABL (Figs. 15b1), limiting low-level ascent and vertical moisture
405 flux (Fig. 15c1). Ascent becomes elevated above 2 km and displaced 4–6 km ahead of the diffuse
406 CPLE after 160 min (denoted by “A” in Figs. 15b2,b3), likely forced by an elevated bore
407 propagating faster than the decaying CPLE, which is addressed in Section 6a. Lack of lower-level
408 ascent prevents low-level air parcels from being lifted (to their LFC), including the elevated high-
409 θ_e air, which is now below the region of ascent, contributing to the decay of storm (Figs. 15c2,c3).

410 When the depth of the coldest MABL is reduced, the cold pool is initially more buoyant
411 than the MABL following its descent down the slope (Fig. 16b1). The shallowest MABLs have

412 the smallest inland penetration distance (Fig. 6b), allowing the cold pool to adiabatically warm
413 during its descent down the full length of the slope, without modification by the MABL. A new
414 elevated region of (bore-induced) buoyant acceleration (a_b) forms $\sim 1\text{--}2$ km ahead of the CPLE
415 and atop the stable MABL (centered near 2 km in altitude, indicated by “A” in Figs. 16b1–b3),
416 while the original dw/dt couplet becomes vertically stacked west of the CPLE, as in the CTRL,
417 and no longer plays a role. This elevated buoyant acceleration lifts high- θ_e air available above the
418 MABL into the updraft, as the buoyancy gradient in the lowest 500-m decreases and surface-based
419 ascent decays (Figs. 16b3,c3).

420 Processes are briefly compared for the storm moving over the 1500-m deep, -5-K θ' MABL
421 and the less cold -3-K θ' MABL with the same depth, to highlight the influence of MABL
422 temperature on storm evolution and differences in precipitation noted in Fig. 4. The cold pool
423 remains less buoyant than the -3-K θ' MABL following its descent downslope, allowing for
424 continued convergence and surface-based upward acceleration at the CPLE at sea level (denoted
425 by “A” in Figs. 17b1–b3), as for the CTRL storm; However, elevated buoyant acceleration forms
426 above the MABL (denoted by “B” in Figs. 17b1–b3), as for the storms over the coldest MABLs.
427 Therefore, when MABLs are more buoyant/warmer than the incoming cold pool, surface-based
428 ascent remains due to the continued presence of a low-level θ_e gradient, while elevated ascent
429 develops due to the relative stability of the layer helping to support bore activity. The conjunction
430 of these two maxima yields deep vertical motion at the CPLE (Figs. 17c1–c3). Though the lower-
431 θ_e MABL air is lifted into the updraft by the surface-based inertial acceleration (a_i), any potentially
432 negative impact on storm survival may be mitigated by the influx of high- θ_e from above the MABL
433 by the elevated buoyant process (a_b), contributing to the maintenance of the storm at the plateau
434 base.

435 **6. Discussion**

436 *a. The development and role of bores*

437 Bores have been shown to form following the collision of a squall line's cold pool and a
438 MABL in coastal regions with no terrain relief, capable of supporting convection offshore over the
439 stable layer MABL (LK18; Lombardo 2020). For squall lines over mountainous coastal regions,
440 similar processes occur following the cold pool-MABL collision. Lifting is supported by an
441 internal bore once storms arrive at sea level and move over the full depth of the MABL, evidenced
442 by elevated buoyant accelerations above the MABL east of the CPLE (Figs. 15b2–3,16b2–3,
443 17b2–3), and a semi-permanent dome in buoyancy (θ not shown) west of the CPLE (Figs. 15a2–
444 3,16a2–3). While these bores can provide a mechanism to lift high- θ_e air located above the MABL
445 into the updraft, storm maintenance is, in part, determined by the availability of this elevated
446 unstable air. Deeper, colder MABLs reduce and can eliminate the elevated high- θ_e layer, promoting
447 storm decay, despite the presence of bore-generated elevated lift.

448 Bores have also been shown to form when squall lines descend the lee slope of an idealized
449 bell-shaped mountain and encounter a stationary, nocturnal stable layer (Letkewicz and Parker
450 2011). With no stable layer downstream of the mountain, convection was suppressed over the lee
451 slope, leading to a precipitation shadow, as in our CTRL simulation. With a lee-side nocturnal
452 stable layer included, convection initiated over the slope as bore-driven lifting developed, and the
453 lee precipitation shadow diminished. Once the nocturnal storms moved away from the mountain,
454 those over the coldest nocturnal layers decayed fastest due to the reduction in available instability,
455 as for our storms over the colder, deeper MABLs. In contrast, for our coastal storms, bores only
456 form once the storms move away from the slope, and the leeside precipitation enhancements are
457 due to the cold-pool-driven processes rather than the bore-induced lifting. Such differences may

458 be attributed to the motion of stable layer (stationary nocturnal vs. moving MABL), the thermal
459 deficit and depth of the stable layer, the terrain characteristics (height, slope angle and distance,
460 bell vs. plateau concavity), and the base-state environment (CAPE, vertical wind shear). One
461 commonality between the studies is that an enhancement in precipitation over the downslope does
462 not indicate a longer-lived squall line.

463 The presence of coastal terrain impacts the generation and utility of bores in supporting
464 offshore deep convection, thus the lifetime of a storm offshore, compared to storms over flat
465 coastal land. Lombardo (2020) showed for squall lines exclusively at sea level, initiated in the
466 same base-state thermodynamic-kinematic environment and with the same CI forcing at $t = 0$ as
467 the present study, the collision of a storm's cold pool and a $-6\text{-K-}\theta'$, 1500-m deep MABL produced
468 relatively strong bore-induced ascent capable of supporting an intense storm hundreds of
469 kilometers offshore. This is in direct contrast to the storm colliding with the $-5\text{-K-}\theta'$, 1500-m deep
470 MABL in the present study, which decayed within 20 km of the terrain base. We hypothesize that
471 such differences may be a consequence of (1) differences in MABL depth at the time of collision,
472 which is larger over flat-land than over the sloping terrain, (2) differences in cold pool buoyancy
473 and depth at the time of collision, with shallower, more buoyant cold pools over the downward
474 sloping terrain, (3) the angle of interaction between the cold pool and MABL, and (4) differences
475 that arise between simulations performed in 2-D (this study) and 3-D (Lombardo 2020).
476 Additional research is required to more deeply understand differences in coastal storm processes
477 for those in the presence and absence of coastal terrain relief.

478 *b. RKW approach to evaluate squall line structure in a mountainous coastal environment*

479 Previous studies have applied a vorticity budget analysis to determine the vertical
480 orientation of ascent over the depth of the cold pool, thus updraft orientation and storm lifetime

481 (Rotunno et al. 1988; Weisman 1992; Weisman and Rotunno 2004). Here, we illustrate the
 482 connection between this approach and the pressure perturbation analysis presented above, toward
 483 a unified theory on squall line evolution in complex environments, namely in the presence of
 484 orographic and low-level atmospheric variability. We begin with RKW's equation 5 (Rotunno et
 485 al. 1988; see also equation 5 in Weisman 1992), which is based on the two-dimensional vorticity
 486 and mass-continuity equations integrated over a box centered on the CPLE in a coordinate system
 487 that moves at the speed of the CPLE:

$$488 \quad \underbrace{\frac{\partial}{\partial t} \int_L^R \int_0^H \eta dz dx}_{\text{tendency}} = \underbrace{\int_0^H (u\eta)_L dz}_{\text{flux at left}} - \underbrace{\int_0^H (u\eta)_R dz}_{\text{flux at right}} - \underbrace{\int_L^R (w\eta)_H dx}_{\text{flux at top}} + \underbrace{\int_0^H (B_L - B_R) dz}_{\text{net baroclinic generation}}, \quad (1)$$

489 where L is the left boundary, R is the right boundary, H is the top of cold pool, u is the horizontal
 490 velocity relative to the speed of the CPLE, w is the vertical velocity, η is the 2-d horizontal vorticity,
 491 and B_L (B_R) is the buoyancy west (east) of the CPLE. A steady balance is assumed, and the
 492 horizontal vorticity tendency is set to zero (as in Rotunno et al. 1988):

$$493 \quad 0 = \left(\frac{u_{L,H}^2}{2} - \frac{u_{L,0}^2}{2} \right) - \left(\frac{u_{R,H}^2}{2} - \frac{u_{R,0}^2}{2} \right) - \int_L^R (w\eta)_H dx + \int_0^H (B_L - B_R) dz. \quad (2)$$

494 Because an optimal state is sought such that the ambient low-level flow at the CPLE is turned
 495 vertically by the cold pool and exits the top of the cold pool as a symmetric, vertically orientated
 496 jet, the integral of $w\eta$ across the jet is set to zero (Rotunno et al. 1988; Weisman 1992). With no
 497 further assumptions to perform a rigorous evaluation of the vorticity budget, the fundamental RKW
 498 concept is obtained, namely a balanced state between ambient-wind-shear-generated and
 499 baroclinically-generated horizontal vorticity:

$$500 \quad (u_{L,0}^2 - u_{L,H}^2) + 2 \int_0^H -(B_L - B_R) dz = u_{R,0}^2 - u_{R,H}^2. \quad (3)$$

501 The first term on the LHS of Eq. (3) is the vorticity associated with storm-relative flow at the left

502 boundary, and second is vorticity generated by baroclinic processes. The RHS of Eq. (3) is the
 503 vorticity associated with environmental shear on the right boundary over the depth of the cold pool.
 504 Physically, Eq. (3) includes contributions from the environmental wind shear (Fig. 1), the storm-
 505 relative flow associated with the moving MABL (Fig. 6), the MABL modified ambient buoyancy
 506 (i.e., $B_R \neq 0$; Figs. 8c–10c, 14a–17a), and the storm-relative flow within the cold pool (Figs. 8a–
 507 10a, 14a–17a), all necessary features to consider a mountainous coastal environment. Note that
 508 over the sloping terrain, the near-surface relative flow within the cold pool is gravitationally
 509 accelerated downward (i.e., $u_{L,0} > 0$; Figs. 12a and 13a,d,g), indicating that the cold pool is in
 510 transition from deep (subcritical) to shallow (supercritical) flow (Frame and Markowski 2006). We
 511 define the net baroclinic generation of horizontal vorticity C^2 as

$$512 \quad C^2 = 2 \int_0^H -(B_L - B_R) dz = C_L^2 - C_R^2 \quad (4)$$

513 where C_L^2 (C_R^2) is negative (positive) vorticity generated by cold pool (environmental) buoyancy.
 514 We also define the negative (positive) vorticity associated with shear at the left (right) boundary
 515 as,

$$516 \quad \Delta u_L^2 = u_{L,0}^2 - u_{L,H}^2 \quad (5)$$

517 and

$$518 \quad \Delta u_R^2 = u_{R,0}^2 - u_{R,H}^2, \quad (6)$$

519 respectively. Eq. (3) can then be reduced to

$$520 \quad \underbrace{\Delta u_L^2 + C^2}_{C_J^2} = \Delta u_R^2, \quad (7)$$

521 where the sum of vorticity tendencies west of the CPLE is denoted by C_J^2 . A vertically orientated
 522 jet at the CPLE is obtained when $C_J/\Delta u_R = 1$, while the vertical jet tilts upshear when $C_J/\Delta u_R > 1$

523 and downshear when $C_J/\Delta u_R < 1$, following Rotunno et al. (1988). In general, for our squall lines,
524 Eq. (7) implies that the import of the relative flows within the cold pool ($\Delta u_L^2 > 0$) intensifies the
525 negative vorticity west of the CPLE, so an optimal state requires a larger ambient wind shear east
526 of the CPLE over the depth of cold pool. In contrast, the negatively buoyant MABL ($C_R^2 > 0$) will
527 decrease the integrated buoyancy gradient (C^2), requiring a smaller ambient wind shear.

528 Here, we present the terms in the vorticity budget and the resulting balance predicted by
529 the analysis while storms are over the sloping terrain and over the marine layer at sea level, two
530 important stages in the storms' life cycles. For storms over the terrain, calculations are performed
531 at the time of collision over a 20-km horizontal domain centered on the CPLE, integrated from the
532 height of the terrain surface where the CPLE is located ($z \approx 0.75$ km) to the top of the cold pool (z
533 ≈ 2.25 km) where the buoyancy is near zero (Figs. 7c1–10c1). For the CTRL storm with no MABL,
534 the downslope accelerating surface flow within the cold pool ($u_{L,0}$) and relatively large horizontal
535 buoyancy gradient across the CPLE ($C^2 = C_L^2 - C_R^2$, Table 6) leads to an imbalance of vorticity
536 across the CPLE; Negative vorticity west of the CPLE has a larger magnitude than that of positive
537 vorticity on the east side, dictating an upshear-tilted updraft ($C_J/\Delta u_R = 1.77$, Table 6). This is
538 consistent with the orientation produced in our simulations (Figs. 7a1–c1), and our pressure
539 perturbation analysis; The baroclinically-generated negative pressure perturbation above the cold
540 pool results in the downward acceleration of parcels following their initial ascent at the CPLE,
541 limited parcel ascent, weaker precipitation, and an upshear tilted updraft (Figs. 12a–c).

542 For progressively deeper MABLs, $C_J/\Delta u_R$ values decrease from 1.77–1.17 (Table 6),
543 indicating more upright ascent with increasing MABL depth. This is primarily due to a reduction
544 in the buoyancy gradient across the CPLE (C_J) due to the presence of the relatively dense MABL,
545 and an increase in the ambient wind shear east of the CPLE (Δu_R) associated with stronger upslope

546 flows generated by the moving MABL (Fig. 6). The vertically integrated buoyancy is lowest and
547 the magnitude of the upslope flow is greatest for the deepest MABL. Though fluctuations in the
548 buoyancy of the cold pools (C^2_L) and the relative flow within the cold pools (Δu^2_L) also exist, they
549 do not systematically contribute to the resulting updraft orientations. These results are consistent
550 with those of our pressure perturbation analysis: For progressively deeper MABLs, the reduction
551 in the baroclinically-generated elevated negative pressure perturbation (Figs. 13b,e,h) allows for
552 parcels to accelerate vertically (Figs. 11a–c), leading to more intense precipitation and upright
553 updrafts (Figs. 8–10).

554 Once the cold pools reach sea level, they deepen, intensify, and slow down (Figs. 14a2–
555 17a2), reflected by the larger C^2_L and smaller Δu^2_L (c.f., Table 6 and Table 7). As such, the
556 dominant contributor to negative vorticity within the cold pool transitions from kinematic (Δu^2_L)
557 to thermodynamic (C^2 ; Table 7), as in our pressure-decomposition analysis. For the CTRL squall
558 line, the negative vorticity behind the CPLE (C_J) continues to overwhelm the environmental wind
559 shear ($C_J/\Delta u_R = 1.63$; Table 7), and the upshear tilted structure is maintained. This behavior is
560 consistent with the continued presence of the elevated negative vertical acceleration associated
561 with the baroclinically-generated negative pressure perturbation (Fig. 14). The marine layer helps
562 to “correct” this imbalance, as the buoyancy gradient across the CPLE is diminished (C^2) and the
563 ambient wind shear is larger (Δu_R , Table 7). The relative contributions of the vorticity budget terms,
564 thus $C_J/\Delta u_R$, are sensitive to MABL depth and density, as for the vertical accelerations and pressure
565 perturbations. Comparing the shallow, cold (500-m deep, $-5\text{-K } \theta'$) and deep, less cold (1500-m
566 deep, $-3\text{-K } \theta'$) MABLs, values of the buoyancy terms are similar (C^2), given that the buoyancy
567 term is the vertical integral over the depth of the cold pool, i.e., the contribution of a less cold
568 MABL distributed through a greater depth is similar to that of a cold MABL concentrated over a

569 shallow depth. However, the deep MABL drives a stronger near-surface wind (Δu_R ; Fig. 6), which
570 contributes to more upright ascent ($C_J/\Delta u_R = 0.98$; Fig. 17) compared to the shallow MABL
571 ($C_J/\Delta u_R = 0.98$; Fig. 17). This is consistent with the greater surface-based inertial acceleration (a_i)
572 observed at the CPLE due to enhanced convergence in the presence of the deep, but less cold
573 MABL (c.f., Figs. 16 and 17).

574 For the squall line encountering the coldest, deepest MABL, the cold pool becomes
575 elevated (Figs. 8a2–c2; e.g., Hitchcock and Schumacher 2020; Parsons et al. 2019; Grasmick et al.
576 2018; Haghi et al. 2019), requiring an upward shift in the bottom boundary of the vorticity budget
577 analysis (e.g., $z = 0.5$ km above sea level), with the MABL serving as a lower boundary. Similar
578 conclusions were reached using a bottom boundary of 0.4 to 0.7 km, i.e., within the moving MABL.
579 Regardless of the vertical displacement, the reduction in the horizontal buoyancy gradient across
580 the CPLE and wind shear within the cold pool limits the negative vorticity production west of the
581 CPLE ($C_J = 9.11$), leading to a downstream tilted structure ($C_J/\Delta u = 0.93$, Table 7; Fig. 15a2).
582 However, at this time, the CI mechanism transitions from a surface-based cold-pool to an elevated
583 bore.

584 7. Conclusions

585 Coastal mid-latitude squall line evolution was evaluated in the presence of plateau-shaped
586 orography, a common coastal terrain configuration in regions with squall line activity. Most
587 importantly, this work identified and quantified the dominant physical mechanisms responsible for
588 precipitation enhancement over the plateau slope as storms descend from the plateau top toward
589 the moving MABL, contributing to observed coastal rain maxima. A summary schematic of the
590 associated processes is provided in Fig. 18. Specifically, the collision of a storm's cold pool and
591 an slope-ascending MABL drives an upward acceleration of lower-buoyancy marine boundary

592 layer air parcels, whose vertical displacement directly impacts precipitation amount and intensity.
593 A parcel's vertical displacement is determined by the magnitude and location of a negative non-
594 hydrostatic inertial pressure perturbation ($p'_{i(nh)}$) behind the gust front, which forms through the
595 baroclinic-generation of horizontal vorticity behind the CPLE. For large horizontal gradients in
596 buoyancy across the gust front (e.g., 500-m deep MABL), an elevated, but low-level, negative
597 $p'_{i(nh)}$ induces a downward acceleration of air parcels following the initial cold pool lift, leading to
598 shallow ascent and less precipitation (Fig. 18a). Presence of a cold, deep MABL reduces the
599 horizontal buoyancy gradient across the gust front, leading to smaller baroclinically-generated
600 horizontal vorticity behind the gust front, thus a smaller pressure perturbation and weaker
601 downward vertical acceleration (Fig. 18b). Consequently, parcels ascend to higher altitudes along
602 more upright trajectories leading to more overall precipitation and a greater rain rate. The
603 magnitude of this horizontal vorticity is sensitive to MABL depth, with less vorticity, a smaller
604 negative $p'_{i(nh)}$, and a smaller negative vertical acceleration for deeper MABLs. Therefore,
605 precipitation over the slope is more intense in the presence of deep MABLs, in spite of the smaller
606 surface-based instability.

607 As the squall lines move away from the terrain, those over the deepest MABLs decay most
608 rapidly, while those over the shallowest decay last, predominantly related to the availability of
609 elevated instability. MABL depth dictates the height of the elevated forcing that forms as storms
610 move over a MABL, and thus the amount of warm, moist air above the MABL that is drawn into
611 the storm (Figs. 18c,d). Low-level θ_e is reduced in the presence of the MABL, and more
612 importantly, deeper MABLs diminish larger amounts of elevated instability available to the storm,
613 promoting more rapid storm decay. Further, MABL temperature determines whether a storm
614 retains a surface-based component (e.g., $-3\text{-K } \theta'$) or becomes completely elevated (e.g., $-5\text{-K } \theta'$).

638

639

APPENDIX

640

Decomposition of Vertical Accelerations and Pressure Perturbations

641

The anelastic momentum equation (JR15) can be written as

642

$$\bar{\rho} \frac{d\mathbf{v}}{dt} = -\nabla p - \rho g \mathbf{k}, \quad (\text{A1})$$

643

where $\bar{\rho}$ is the base-state density including all hydrometeors, $\mathbf{v} = (u, v, w)$ is the wind field, p is

644

pressure, g is the gravitational acceleration, and ∇p is the pressure gradient. Total p and ρ can be

645

divided into a horizontally homogeneous base-state value and a deviation from the base state,

646

$$p(x, y, z, t) = \bar{p}(z) + p'(x, y, z, t) \quad (\text{A2})$$

647

and

648

$$\rho(x, y, z, t) = \bar{\rho}(z) + \rho'(x, y, z, t) \quad (\text{A3})$$

649

where the base state (perturbation) is denoted with overbar (prime).

650

Introducing Eqs. (A2) and (A3) to Eq. (A1) and applying the hydrostatic balance, the

651

anelastic momentum equation can be rewritten in the form of perturbation as

652

$$\bar{\rho} \frac{d\mathbf{v}}{dt} = -\nabla p' - \rho' g \mathbf{k} \quad (\text{A4})$$

653

which can be expressed as

654

$$\frac{\partial \mathbf{v}}{\partial t} + \mathbf{v} \cdot \nabla \mathbf{v} = -\alpha_0 \nabla p' + B \mathbf{k}, \quad (\text{A5})$$

655

where $B = -(\rho' / \bar{\rho}) g$ is buoyancy, $\alpha_0 \equiv 1 / \bar{\rho}$ is specific volume.

656

The pressure perturbation can be decomposed into a hydrostatic (p'_h) and nonhydrostatic

657

p'_{nh} component,

658
$$p' = p'_h + p'_{nh}, \quad (\text{A6})$$

659 where p'_h can be related to ρ' as $\partial p'_h / \partial z = -\rho' g$. Applying Eq. (A6) to Eq. (A5) yields

660
$$\frac{\partial \mathbf{v}}{\partial t} + \mathbf{v} \cdot \nabla \mathbf{v} = -\alpha_0 (\nabla p'_{nh} + \nabla_h p'_h). \quad (\text{A7})$$

661 Therefore, the vertical component of Eq. (A7) is

662
$$\frac{dw}{dt} = \frac{\partial w}{\partial t} + \mathbf{v} \cdot \nabla w = -\alpha_0 \frac{\partial p'_{nh}}{\partial z}, \quad (\text{A8})$$

663 which indicates that vertical acceleration is from the nonhydrostatic perturbation pressure gradient

664 force (NPPGF), which can be solved for by taking the divergence of Eq. (A7) and applying the

665 anelastic mass continuity $\nabla \cdot (\bar{\rho} \mathbf{v}) = 0$, yielding the Poisson Equation (PE) about p'_{nh} ,

666
$$-\nabla^2 p'_{nh} = \nabla \cdot (\bar{\rho} \mathbf{v} \cdot \nabla \mathbf{v}) + \nabla_h^2 p'_h, \quad (\text{A9})$$

667 where ∇^2 (∇_h^2) is the 3D (2D) Laplace operator. Applying $-\partial_z$ of Eq. (A9) to Eq. (A8) yields a

668 similar form of the vertical equation to JR15

669
$$-\nabla^2 \left(\bar{\rho} \frac{dw}{dt} \right) = -\partial_z \nabla \cdot (\bar{\rho} \mathbf{v} \cdot \nabla \mathbf{v}) + g \nabla_h^2 \rho'. \quad (\text{A10})$$

670 Following JR15, we define the buoyant acceleration (a_b) as the vertical acceleration if the wind

671 field is instantaneously zero,

672
$$a_b \equiv \left. \frac{dw}{dt} \right|_{\mathbf{v}=0}, \quad (\text{A11})$$

673 and the inertial acceleration (a_i) if the horizontal density anomalies are instantly zero,

674
$$a_i \equiv \left. \frac{dw}{dt} \right|_{\rho=\bar{\rho}}. \quad (\text{A12})$$

675 Applying Eq. (A11) to Eq. (A10) yields the PE about a_b ,

676
$$-\nabla^2 (\bar{\rho} a_b) = g \nabla_h^2 \rho', \quad (\text{A13})$$

677 and applying Eq. (A12) to Eq. (A10) yields the PE about a_i ,

$$678 \quad -\nabla^2 (\bar{\rho} a_i) = -\partial_z \nabla \cdot (\bar{\rho} \mathbf{v} \cdot \nabla \mathbf{v}). \quad (\text{A14})$$

679 As w maintains zero at bottom and top boundaries, the PEs of Eqs. (A10), (A13) and (A14)

680 have the same Dirichlet boundary conditions (BCs). Since $\bar{\rho} \frac{dw}{dt}$ and $(\bar{\rho} a_b + \bar{\rho} a_i)$ obey the same

681 PE and BCs,

$$682 \quad \frac{dw}{dt} = a_b + a_i. \quad (\text{A15})$$

683 Therefore, a similar decomposition of vertical acceleration as in JR15 can be derived by using

684 perturbation variables.

685 With NPPGF the only source of vertical acceleration, decomposition of p'_{nh} is more

686 intuitive to quantify the contributions to vertical motion. Definitions of Eqs. (A11) and (A12) are

687 extended to p'_{nh} , with the buoyant pressure perturbation $p'_{b(nh)}$ define as

$$688 \quad p'_{b(nh)} \equiv p'_{nh} \Big|_{\mathbf{v}=0}, \quad (\text{A16})$$

689 and the inertial pressure perturbation $p'_{i(nh)}$ defined as

$$690 \quad p'_{i(nh)} \equiv p'_{nh} \Big|_{\rho=\bar{\rho}}. \quad (\text{A17})$$

691 Applying Eqs. (A16) and (A17) to Eq. (A9) yields the PEs about $p'_{b(nh)}$ and $p'_{i(nh)}$,

$$692 \quad -\nabla^2 p'_{b(nh)} = \nabla_h^2 p'_h \quad (\text{A18})$$

693 and

$$694 \quad -\nabla^2 p'_{i(nh)} = \nabla \cdot (\bar{\rho} \mathbf{v} \cdot \nabla \mathbf{v}). \quad (\text{A19})$$

695 Taking $-\partial_z$ of Eqs. (A18) and (A19) yields

$$696 \quad -\nabla^2 \left(-\partial_z p'_{b(nh)} \right) = g \nabla_h^2 \rho', \quad (\text{A20})$$

697 and

698
$$-\nabla^2 \left(-\partial_z p'_{i(nh)} \right) = -\partial_z \nabla \cdot (\bar{\rho} \mathbf{v} \cdot \nabla \mathbf{v}). \quad (\text{A21})$$

699 Comparing with Eq. (A20) with Eq. (A13), $-\partial_z p'_{b(nh)}$ and $\bar{\rho} a_b$ obey the same PE and BC,
700 which implies

701
$$a_b = -\alpha_0 \frac{\partial}{\partial z} p'_{b(nh)}, \quad (\text{A22})$$

702 and comparing Eq. (A21) with Eq. (A14),

703
$$a_i = -\alpha_0 \frac{\partial}{\partial z} p'_{i(nh)}. \quad (\text{A23})$$

704 Therefore, $p'_{b(nh)}$ [$p'_{i(nh)}$] is the part of p'_{nh} responsible for a_b (a_i). Plugging Eqs. (A22) and (A23)
705 into Eq. (A15) and applying Eqs. (A8), (A16), and (A17), we obtain the decomposition of p'_{nh} ,

706
$$p'_{nh} = p'_{b(nh)} + p'_{i(nh)}. \quad (\text{A24})$$

707 As p' can also be decomposed into a buoyant (p'_B) and dynamic [p'_d , Markowski and
708 Richardson 2011; i.e., $p'_{i(nh)}$ in this work] pressure perturbation, combining Eqs. (A6) and (A24)
709 yields $p'_{b(nh)} = p'_B - p'_h$, implying that $p'_{b(nh)}$ is the “effective” portion of p'_B due the compensation
710 for p'_h .

711 Following Klemp and Rotunno (1983), the RHS of Eq. (A19) can be expanded as

712
$$-\alpha_0 \nabla^2 p'_{i(nh)} = e_{ij}^2 - \frac{1}{2} |\boldsymbol{\omega}|^2 - w^2 \frac{d^2 \ln \bar{\rho}}{dz^2}, \quad (\text{A25})$$

713 where $\boldsymbol{\omega}$ is the relative vorticity vector and e_{ij} is the deformation tensor,

714
$$e_{ij}^2 = \frac{1}{4} \sum_{i=1}^3 \sum_{j=1}^3 \left(\frac{\partial u_i}{\partial x_j} + \frac{\partial u_j}{\partial x_i} \right)^2. \quad (\text{A26})$$

715 The terms on the RHS of Eq. (A25) are the deformation of the wind field (*splat* term), the rotation
716 of the wind field (*spin* term), and a minimal term that can be neglected (JR15), respectively. For

717 well-behaved fields [i.e., $\nabla^2 p'_{i(nh)} \propto -p'_{i(nh)}$], the splat (spin) term contributes positively (negatively)
718 to $p'_{i(nh)}$.

719 In our calculation, model output is interpolated to a uniform orthogonal grid with
720 horizontal (vertical) grid spacing of 200 (50) m. The Eqs. (A13) and (A14) are solved numerically
721 using the fast Fourier transform method (Fuka 2015), as well as Eq. (A19), though it is somewhat
722 arbitrary to specify the constant added to the $p'_{i(nh)}$ solution due to the unknown BCs. Therefore,
723 we use the same constraint as the CM1 to determine the constant, which is that the domain-
724 averaged $p'_{i(nh)}$ field at the model top is zero; $p'_{b(nh)}$ is solved similarly. The p'_h is calculated by
725 subtracting p'_{nh} from the total p' output from the model.

726

727

REFERENCES

- 728 Banacos, P. C., and D. M. Schultz, 2005: The use of moisture flux convergence in forecasting
729 convective initiation: Historical and operational perspectives. *Wea. Forecasting*, **20**, 351–366,
730 <https://doi.org/10.1175/WAF858.1>.
- 731 Bergemann, M., C. Jakob, and T. P. Lane, 2015: Global detection and analysis of coastline-
732 associated rainfall using an objective pattern recognition technique. *J. Climate*, **28**, 7225–
733 7236, <https://doi.org/10.1175/JCLI-D-15-0098.1>.
- 734 Bryan, G. H., and J. M. Fritsch, 2002: A benchmark simulation for moist nonhydrostatic numerical
735 models. *Mon. Wea. Rev.*, **130**, 2917–2928, [https://doi.org/10.1175/1520-0493\(2002\)130<2917:ABSFMN>2.0.CO;2](https://doi.org/10.1175/1520-0493(2002)130<2917:ABSFMN>2.0.CO;2).
- 737 ———, and R. Rotunno, 2014: The optimal state for gravity currents in shear. *J. Atmos. Sci.*, **71**,
738 448–468, <https://doi.org/10.1175/JAS-D-13-0156.1>.
- 739 Cafaro, C., and G. G. Rooney, 2018: Characteristics of colliding density currents: A numerical and

740 theoretical study. *Quart. J. Roy. Meteor. Soc.*, **144**, 1761–1771,
741 <https://doi.org/10.1002/qj.3337>.

742 Carbone, R. E., J. W. Conway, N. A. Crook, and M. W. Moncrieff, 1990: The generation and
743 propagation of a nocturnal squall line. Part I: Observations and implications for mesoscale
744 predictability. *Mon. Wea. Rev.*, **118**, 26–49, [https://doi.org/10.1175/1520-0493\(1990\)118<0026:TGAPOA>2.0.CO;2](https://doi.org/10.1175/1520-0493(1990)118<0026:TGAPOA>2.0.CO;2).

746 Cecil, D. J., and E. J. Zipser, 1999: Relationships between tropical cyclone intensity and satellite-
747 based indicators of inner core convection: 85-GHz ice-scattering signature and lightning. *Mon.*
748 *Wea. Rev.*, **127**, 103–123, [https://doi.org/10.1175/1520-0493\(1999\)127<0103:RBTICIA>2.0.CO;2](https://doi.org/10.1175/1520-0493(1999)127<0103:RBTICIA>2.0.CO;2).

750 Cohuet, J. B., R. Romero, V. Homar, V. Ducrocq, and C. Ramis, 2011: Initiation of a severe
751 thunderstorm over the Mediterranean Sea. *Atmos. Res.*, **100**, 603–620,
752 <https://doi.org/10.1016/j.atmosres.2010.11.002>.

753 Curtis, S., 2019: Means and long-Term trends of global coastal zone precipitation. *Sci. Rep.*, **9**, 1–
754 9, <https://doi.org/10.1038/s41598-019-41878-8>.

755 Dawson, D. T., M. Xue, A. Shapiro, J. A. Milbrandt, and A. D. Schenkman, 2016: Sensitivity of
756 real-data simulations of the 3 May 1999 Oklahoma City tornadic supercell and associated
757 tornadoes to multimoment microphysics. Part II: Analysis of buoyancy and dynamic pressure
758 forces in simulated tornado-like vortices. *J. Atmos. Sci.*, **73**, 1039–1061,
759 <https://doi.org/10.1175/JAS-D-15-0114.1>.

760 Deardorff, J. W., 1980: Stratocumulus-capped mixed layers derived from a three-dimensional
761 model. *Bound.-Layer Meteor.*, **18**, 495–527, <https://doi.org/10.1007/BF00119502>.

762 Droegemeier, K. K., and R. B. Wilhelmson, 1985: Three-dimensional numerical modeling of

763 convection produced by interacting thunderstorm outflows. Part II: Variations in vertical wind
764 shear. *J. Atmos. Sci.*, **42**, 2404–2414, [https://doi.org/10.1175/1520-](https://doi.org/10.1175/1520-0469(1985)042<2404:TDNMOC>2.0.CO;2)
765 [0469\(1985\)042<2404:TDNMOC>2.0.CO;2](https://doi.org/10.1175/1520-0469(1985)042<2404:TDNMOC>2.0.CO;2).

766 Feng, Z., S. Hagos, A. K. Rowe, C. D. Burleyson, M. N. Martini, and S. P. Szoeke, 2015:
767 Mechanisms of convective cloud organization by cold pools over tropical warm ocean during
768 the AMIE/DYNAMO field campaign. *J. Adv. Model. Earth Syst.*, **7**, 357–381,
769 <https://doi.org/10.1002/2014MS000384>.

770 Frame, J. W., and P. Markowski, 2006: The interaction of simulated squall lines with idealized
771 mountain ridges. *Mon. Wea. Rev.*, **134**, 1919–1941, <https://doi.org/10.1175/MWR3157.1>.

772 Fuka, V., 2015: PoisFFT - A free parallel fast Poisson solver. *Appl. Math. Comput.*, **267**, 356–364,
773 <https://doi.org/10.1016/j.amc.2015.03.011>.

774 Gal-Chen, T., and R. C. J. Somerville, 1975: On the use of a coordinate transformation for the
775 solution of the Navier-Stokes equations. *J. Comput. Phys.*, **17**, 209–228,
776 [https://doi.org/10.1016/0021-9991\(75\)90037-6](https://doi.org/10.1016/0021-9991(75)90037-6).

777 Grant, L. D., and S. C. van den Heever, 2016: Cold pool dissipation. *J. Geophys. Res. Atmos.*, **121**,
778 1138–1155, <https://doi.org/10.1002/2015JD023813>.

779 Grasmick, C., B. Geerts, D. D. Turner, Z. Wang, and T. M. Weckwerth, 2018: The Relation between
780 Nocturnal MCS Evolution and Its Outflow Boundaries in the Stable Boundary Layer: An
781 Observational Study of the 15 July 2015 MCS in PECAN. *Mon. Wea. Rev.*, **146**, 3203–3226,
782 <https://doi.org/10.1175/MWR-D-18-0169.1>.

783 Haghi, K. R., and Coauthors, 2019: Bore-ing into Nocturnal Convection. *Bull. Amer. Meteor. Soc.*,
784 **100**, 1103–1121, <https://doi.org/10.1175/BAMS-D-17-0250.1>.

785 Hitchcock, S. M., and R. S. Schumacher, 2020: Analysis of Back-Building Convection in

786 Simulations with a Strong Low-Level Stable Layer. *Mon. Wea. Rev.*, **148**, 3773–3797,
787 <https://doi.org/10.1175/MWR-D-19-0246.1>.

788 Huang, Y., Y. Liu, Y. Liu, and J. C. Knievel, 2019: Budget analyses of a record-breaking rainfall
789 event in the coastal metropolitan city of Guangzhou, China. *J. Geophys. Res. Atmos.*, **124**,
790 9391–9406, <https://doi.org/10.1029/2018JD030229>.

791 Jeevanjee, N., and D. M. Romps, 2015: Effective buoyancy, inertial pressure, and the mechanical
792 generation of boundary layer mass flux by cold pools. *J. Atmos. Sci.*, **72**, 3199–3213,
793 <https://doi.org/10.1175/JAS-D-14-0349.1>.

794 Kingsmill, D. E., 1995: Convection initiation associated with a sea-breeze front, a gust front, and
795 their collision. *Mon. Wea. Rev.*, **123**, 2913–2933, [https://doi.org/10.1175/1520-0493\(1995\)123<2913:CIAWAS>2.0.CO;2](https://doi.org/10.1175/1520-0493(1995)123<2913:CIAWAS>2.0.CO;2).

797 Klemp, J. B., and R. Rotunno, 1983: A study of the tornadic region within a supercell thunderstorm.
798 *J. Atmos. Sci.*, **40**, 359–377, [https://doi.org/10.1175/1520-0469\(1983\)040<0359:ASOTTR>2.0.CO;2](https://doi.org/10.1175/1520-0469(1983)040<0359:ASOTTR>2.0.CO;2).

800 Kömüştü, A. Ü., A. Erkan, and S. Çelik, 1998: Analysis of meteorological and terrain features
801 leading to the Izmir flash flood, 3–4 November 1995. *Nat. Hazards*, **18**, 1–25,
802 <https://doi.org/10.1023/A:1008078920113>.

803 Letkewicz, C. E., and M. D. Parker, 2010: Forecasting the maintenance of mesoscale convective
804 systems crossing the appalachian mountains. *Wea. Forecasting*, **25**, 1179–1195,
805 <https://doi.org/10.1175/2010WAF2222379.1>.

806 ———, and ———, 2011: Impact of environmental variations on simulated squall lines interacting
807 with terrain. *Mon. Wea. Rev.*, **139**, 3163–3183, <https://doi.org/10.1175/2011MWR3635.1>.

808 Li, Y., and R. E. Carbone, 2015: Offshore propagation of coastal precipitation. *J. Atmos. Sci.*, **72**,

809 4553–4568, <https://doi.org/10.1175/JAS-D-15-0104.1>.

810 Lombardo, K. A., 2020: Squall Line Response to Coastal Mid-Atlantic Thermodynamic
811 Heterogeneities. *J. Atmos. Sci.*, **77**, 4143–4170, <https://doi.org/10.1175/JAS-D-20-0044.1>.

812 —, and B. A. Colle, 2011: Convective storm structures and ambient conditions associated with
813 severe weather over the northeast United States. *Wea. Forecasting*, **26**, 940–956,
814 <https://doi.org/10.1175/WAF-D-11-00002.1>.

815 —, and —, 2012: Ambient conditions associated with the maintenance and decay of quasi-
816 linear convective systems crossing the northeastern U.S. coast. *Mon. Wea. Rev.*, **140**, 3805–
817 3819, <https://doi.org/10.1175/MWR-D-12-00050.1>.

818 —, and —, 2013: Processes controlling the structure and longevity of two quasi-linear
819 convective systems crossing the southern new england coast. *Mon. Wea. Rev.*, **141**, 3710–
820 3734, <https://doi.org/10.1175/MWR-D-12-00336.1>.

821 —, and T. Kading, 2018: The behavior of squall lines in horizontally heterogeneous coastal
822 environments. *J. Atmos. Sci.*, **75**, 1243–1269, <https://doi.org/10.1175/JAS-D-17-0248.1>.

823 López, M. E., and W. E. Howell, 1967: Katabatic winds in the equatorial Andes. *J. Atmos. Sci.*, **24**,
824 29–35, [https://doi.org/10.1175/1520-0469\(1967\)024<0029:KWITEA>2.0.CO;2](https://doi.org/10.1175/1520-0469(1967)024<0029:KWITEA>2.0.CO;2).

825 Mapes, B. E., T. T. Warner, and M. Xu, 2003: Diurnal patterns of rainfall in Northwestern South
826 America. Part III: Diurnal gravity waves and nocturnal convection offshore. *Mon. Wea. Rev.*,
827 **131**, 830–844, [https://doi.org/10.1175/1520-0493\(2003\)131<0830:DPORIN>2.0.CO;2](https://doi.org/10.1175/1520-0493(2003)131<0830:DPORIN>2.0.CO;2).

828 Markowski, P., and Y. Richardson, 2011: *Mesoscale Meteorology in Midlatitudes*. John Wiley &
829 Sons, 430 pp.

830 Markowski, P. M., 2016: An idealized numerical simulation investigation of the effects of surface
831 drag on the development of near-surface vertical vorticity in supercell thunderstorms. *J.*

832 *Atmos. Sci.*, **73**, 4349–4385, <https://doi.org/10.1175/JAS-D-16-0150.1>.

833 Moncrieff, M. W., and C. Liu, 1999: Convection initiation by density currents: Role of
834 convergence, shear, and dynamical organization. *Mon. Wea. Rev.*, **127**, 2455–2464,
835 [https://doi.org/10.1175/1520-0493\(1999\)127<2455:CIBDCR>2.0.CO;2](https://doi.org/10.1175/1520-0493(1999)127<2455:CIBDCR>2.0.CO;2).

836 Morrison, H., G. Thompson, and V. Tatarskii, 2009: Impact of cloud microphysics on the
837 development of trailing stratiform precipitation in a simulated squall line: Comparison of one-
838 and two-moment schemes. *Mon. Wea. Rev.*, **137**, 991–1007,
839 <https://doi.org/10.1175/2008MWR2556.1>.

840 ———, J. A. Milbrandt, G. H. Bryan, K. Ikeda, S. A. Tessendorf, and G. Thompson, 2015:
841 Parameterization of cloud microphysics based on the prediction of bulk ice particle properties.
842 Part II: Case study comparisons with observations and other schemes. *J. Atmos. Sci.*, **72**, 312–
843 339, <https://doi.org/10.1175/JAS-D-14-0066.1>.

844 Ogino, S. Y., M. D. Yamanaka, S. Mori, and J. Matsumoto, 2016: How much is the precipitation
845 amount over the tropical coastal region? *J. Climate*, **29**, 1231–1236,
846 <https://doi.org/10.1175/JCLI-D-15-0484.1>.

847 Parsons, D. B., K. R. Haghi, K. T. Halbert, B. Elmer, and J. Wang, 2019: The Potential Role of
848 Atmospheric Bores and Gravity Waves in the Initiation and Maintenance of Nocturnal
849 Convection over the Southern Great Plains. *J. Atmos. Sci.*, **76**, 43–68,
850 <https://doi.org/10.1175/JAS-D-17-0172.1>.

851 Peters, J. M., 2016: The impact of effective buoyancy and dynamic pressure forcing on vertical
852 velocities within two-dimensional updrafts. *J. Atmos. Sci.*, **73**, 4531–4551,
853 <https://doi.org/10.1175/JAS-D-16-0016.1>.

854 Pucillo, A., M. M. Miglietta, K. Lombardo, and A. Manzato, 2019: Application of a simple

855 analytical model to severe winds produced by a bow echo like storm in northeast Italy. *Meteor.*
856 *Appl.*, 1–18, <https://doi.org/10.1002/met.1868>.

857 Reeves, H. D., and Y. L. Lin, 2007: The effects of a mountain on the propagation of a preexisting
858 convective system for blocked and unblocked flow regimes. *J. Atmos. Sci.*, **64**, 2401–2421,
859 <https://doi.org/10.1175/JAS3959.1>.

860 Rotunno, R., J. B. Klemp, and M. L. Weisman, 1988: A theory for strong, long-lived squall lines.
861 *J. Atmos. Sci.*, **45**, 463–485, [https://doi.org/10.1175/1520-](https://doi.org/10.1175/1520-0469(1988)045<0463:ATFSSL>2.0.CO;2)
862 [0469\(1988\)045<0463:ATFSSL>2.0.CO;2](https://doi.org/10.1175/1520-0469(1988)045<0463:ATFSSL>2.0.CO;2).

863 Schenkman, A. D., M. Xue, and D. T. Dawson, 2016: The cause of internal outflow surges in a
864 high-resolution simulation of the 8 May 2003 Oklahoma City tornadic supercell. *J. Atmos.*
865 *Sci.*, **73**, 353–370, <https://doi.org/10.1175/JAS-D-15-0112.1>.

866 Smith, V. H., S. D. Mobbs, R. R. Burton, M. Hobby, F. Aoshima, V. Wulfmeyer, and P. Di Girolamo,
867 2014: The role of orography in the regeneration of convection: A case study from the
868 convective and orographically-induced precipitation study. *Meteor. Zeitschrift*, **24**, 83–97,
869 <https://doi.org/10.1127/metz/2014/0418>.

870 Soderholm, J., H. McGowan, H. Richter, K. Walsh, T. Weckwerth, and M. Coleman, 2016: The
871 coastal convective interactions experiment (CCIE): Understanding the role of sea breezes for
872 hailstorm hotspots in Eastern Australia. *Bull. Amer. Meteor. Soc.*, **97**, 1687–1698,
873 <https://doi.org/10.1175/BAMS-D-14-00212.1>.

874 de Szoeki, S. P., E. D. Skyllingstad, P. Zuidema, and A. S. Chandra, 2017: Cold pools and their
875 influence on the tropical marine boundary layer. *J. Atmos. Sci.*, **74**, 1149–1168,
876 <https://doi.org/10.1175/JAS-D-16-0264.1>.

877 Teng, J. H., C. Sen Chen, T. C. C. Wang, and Y. L. Chen, 2000: Orographic effects on a squall line

878 system over Taiwan. *Mon. Wea. Rev.*, **128**, 1123–1138, <https://doi.org/10.1175/1520->
879 0493(2000)128<1123:OEOASL>2.0.CO;2.

880 Tompkins, A. M., 2001: Organization of tropical convection in low vertical wind shears: The role
881 of water vapor. *J. Atmos. Sci.*, **58**, 529–545, <https://doi.org/10.1175/1520->
882 0469(2001)058<0529:OOTCIL>2.0.CO;2.

883 Torri, G., Z. Kuang, and Y. Tian, 2015: Mechanisms for convection triggering by cold pools.
884 *Geophys. Res. Lett.*, **42**, 1943–1950, <https://doi.org/10.1002/2015GL063227>.

885 Trapp, R. J., and M. L. Weisman, 2003: Low-level mesovortices within squall lines and bow echoes.
886 Part II: Their genesis and implications. *Mon. Wea. Rev.*, **131**, 2804–2823,
887 [https://doi.org/10.1175/1520-0493\(2003\)131<2804:LMWSLA>2.0.CO;2](https://doi.org/10.1175/1520-0493(2003)131<2804:LMWSLA>2.0.CO;2).

888 Warner, T. T., B. E. Mapes, and M. Xu, 2003: Diurnal patterns of rainfall in northwestern South
889 America. Part II: Model simulations. *Mon. Wea. Rev.*, **131**, 813–829,
890 [https://doi.org/10.1175/1520-0493\(2003\)131<0813:DPORIN>2.0.CO;2](https://doi.org/10.1175/1520-0493(2003)131<0813:DPORIN>2.0.CO;2).

891 Weisman, M. L., 1992: The Role of Convectively Generated Rear-Inflow Jets in the Evolution of
892 Long-Lived Mesoconvective Systems. *J. Atmos. Sci.*, **49**, 1826–1847,
893 [https://doi.org/10.1175/1520-0469\(1992\)049<1826:TROCGR>2.0.CO;2](https://doi.org/10.1175/1520-0469(1992)049<1826:TROCGR>2.0.CO;2).

894 —, and R. Rotunno, 2004: “A theory for strong long-lived squall lines” revisited. *J. Atmos. Sci.*,
895 **61**, 361–382, [https://doi.org/10.1175/1520-0469\(2004\)061<0361:ATFSLS>2.0.CO;2](https://doi.org/10.1175/1520-0469(2004)061<0361:ATFSLS>2.0.CO;2).

896 van der Wiel, K., S. T. Gille, S. G. Llewellyn Smith, P. F. Linden, and C. Cenedese, 2017:
897 Characteristics of colliding sea breeze gravity current fronts: a laboratory study. *Quart. J. Roy.*
898 *Meteor. Soc.*, **143**, 1434–1441, <https://doi.org/10.1002/qj.3015>.

899 Wilson, J. W., and W. E. Schreiber, 1986: Initiation of convective storms at radar-observed
900 boundary-layer convergence lines. *Mon. Wea. Rev.*, **114**, 2516–2536,

901 [https://doi.org/10.1175/1520-0493\(1986\)114<2516:IOCSAR>2.0.CO;2](https://doi.org/10.1175/1520-0493(1986)114<2516:IOCSAR>2.0.CO;2).

902 Wu, P., M. Hara, J. I. Hamada, M. D. Yamanaka, and F. Kimura, 2009: Why a large amount of rain
903 falls over the sea in the vicinity of western Sumatra Island during nighttime. *J. Appl. Meteor.*
904 *Climatol.*, **48**, 1345–1361, <https://doi.org/10.1175/2009JAMC2052.1>.

905 Xu, J., and Y. Wang, 2015: A statistical analysis on the dependence of tropical cyclone
906 intensification rate on the storm intensity and size in the North Atlantic. *Wea. Forecasting*,
907 **30**, 692–701, <https://doi.org/10.1175/WAF-D-14-00141.1>.

908 Xu, X., M. Xue, and Y. Wang, 2015: The genesis of mesovortices within a real-data simulation of
909 a bow echo system. *J. Atmos. Sci.*, **72**, 1963–1986, <https://doi.org/10.1175/JAS-D-14-0209.1>.

910 Zuidema, P., G. Torri, C. Muller, and A. Chandra, 2017: A survey of precipitation-induced
911 atmospheric cold pools over oceans and their interactions with the larger-scale environment.
912 *Surv. Geophys.*, **38**, 1283–1305, <https://doi.org/10.1007/s10712-017-9447-x>.

913

914

915

916

917

918

919

920

921

922

923

924 **LIST OF TABLES**

925 TABLE 1. Base-state stability indexes of most unstable convective available potential energy
 926 (MUCAPE, J kg^{-1}), most unstable convective inhibition (MUCIN, J kg^{-1}), surface-based
 927 convective available potential energy (SBCAPE, J kg^{-1}), surface-based convective inhibition
 928 (SBCIN, J kg^{-1}), lifting condensation level (LCL, m, AGL), and level of free convection (LFC, m,
 929 AGL) on the plateau, on the slope, and at sea level. All values are from single-point locations.....44

930
 931 TABLE 2. Base-state SBCAPE (J kg^{-1}) and MUCAPE (J kg^{-1}) at the plateau base (360–800 km)
 932 for the experiments with a MABL, with depths of 500 m, 1000 m, and 1500 m and potential
 933 temperature perturbations (θ') of -2 K , -3 K , -4 K , and -5 K relative to the base-state. All values
 934 are from single-point locations. 45

935
 936 TABLE 3. Statistics of the MABL parcels released when the cold pools collide with the coldest
 937 MABLs ($-5\text{-K } \theta'$) with varied depths (indicated by the black contours in Figs. 11a–c), including
 938 buoyancy (B , 10^{-2} m s^{-2}), convective available potential energy (CAPE; J kg^{-1}), and convective
 939 inhibition (CIN; J kg^{-1}) at the release times (112 min, 109 min, and 107 min for 500-m, 1000-m,
 940 and 1500-m deep, respectively), parcel height (z_{10} , km) and vertical velocity (w , m s^{-1}) 10 min
 941 after release. Results are averaged over all MABL air parcels with $B < -0.01\text{ m s}^{-2}$ 46

942
 943 TABLE 4. Statistics of the MABL parcels released when the squall lines are at the plateau base
 944 (indicated by the black contours in Figs. 11d–f), including buoyancy (B , 10^{-2} m s^{-2}), CAPE (J
 945 kg^{-1}), and CIN (J kg^{-1}) at the release time (170 min for all experiments), parcel height (z_{20} , km)
 946 and vertical velocity (w , m s^{-1}) 20 min after release. Results are averaged over all MABL parcels
 947 with B of $[-0.1, -0.01]\text{ m s}^{-2}$. Note that the MABL parcels with $B < -0.1\text{ m s}^{-2}$ are not included in
 948 the statistics to evaluate only parcels that are lifted to the updrafts (Figs. 11d–f)..... 47

949
 950 TABLE 5. Positive vertical acceleration (dw/dt^+ , 10^{-2} m s^{-2}), its buoyant component (a_b^+ , 10^{-2} m
 951 s^{-2}), and inertial component (a_i^+ , 10^{-2} m s^{-2}); negative vertical acceleration (dw/dt^- , 10^{-2} m s^{-2}),
 952 its buoyant component (a_b^- , 10^{-2} m s^{-2}), and inertial component (a_i^- , 10^{-2} m s^{-2}). Positive
 953 (negative) vertical acceleration is a 10-min average after the collision time, for values $\geq 1 \times 10^{-2}\text{ m}$

954 s^{-2} ($\leq -1 \times 10^{-2} \text{ m s}^{-2}$) in an 8-km (horizontal) \times 5-km (vertical) domain centered on the CPLE (see
955 Figs. 12 and 13 for reference). 48

956
957 TABLE 6. Vorticity budget analysis following Rotunno et al. (1988), where C^2 ($\text{m}^2 \text{s}^{-2}$) is the net
958 baroclinic generation of vorticity calculated from $C^2_L - C^2_R$; C^2_L and C^2_R are the baroclinically
959 generated vorticity to the left and right of the CPLE; Δu^2_L are contributions from flows within the
960 cold pool; C_J (m s^{-1}) represents the negative vorticity within the cold pool, including contributions
961 from C^2 and Δu^2_L (Δu^2_L , $\text{m}^2 \text{s}^{-2}$); Δu_R (m s^{-1}) is the ambient wind shear east of the CPLE; $C_J/\Delta u$ is
962 the balance approximation. Values of C^2_L and Δu^2_L (C^2_R and Δu_R) are averaged over 10 km west
963 (east) of the CPLE from the terrain height ($z = 0.75 \text{ km}$) to the top of cold pool ($z = 2.25 \text{ km}$) when
964 the cold pool collides with the upslope flow/moving MABL (107–113 min) on the slope, for the
965 CTRL storm and the those encountering a 500-m deep $-5\text{-K } \theta'$, 1000-m deep $-5\text{-K } \theta'$ MABL,
966 1500-m deep $-5\text{-K } \theta'$ MABL. 49

967
968 TABLE 7. Same as Table 6, but at 160–170 min when the cold pool arrives at the plateau base, for
969 the CTRL storm and the those encountering a 500-m deep $-5\text{-K } \theta'$, 1500-m deep $-3\text{-K } \theta'$ MABL,
970 1500-m deep $-5\text{-K } \theta'$ MABL. For the experiment with 1500-m deep $-5\text{-K } \theta'$ MABL, results are
971 calculated from $z = 0.5\text{--}2.25 \text{ km}$ due to the presence of an elevated cold pool. 50

972

973

974

975

976

977

978

979

980

981

982
983
984
985
986
987

988
989
990
991
992
993
994
995
996
997
998

TABLE 1. Base-state stability indexes of most unstable convective available potential energy (MUCAPE, $J\ kg^{-1}$), most unstable convective inhibition (MUCIN, $J\ kg^{-1}$), surface-based convective available potential energy (SBCAPE, $J\ kg^{-1}$), surface-based convective inhibition (SBCIN, $J\ kg^{-1}$), lifting condensation level (LCL, m, AGL), and level of free convection (LFC, m, AGL) on the plateau, on the slope, and at sea level. All values are from single-point locations.

	Plateau (0–300 km)	Slope (330 km)	Bottom (360–800 km)
MUCAPE ($J\ kg^{-1}$)	917.50	1491.70	1630.53
MUCIN ($J\ kg^{-1}$)	1.61	3.18	17.04
SBCAPE ($J\ kg^{-1}$)	738.69	1382.14	1596.95
SBCIN ($J\ kg^{-1}$)	0.10	0.10	13.01
LCL (m)	363.29	398.28	799.74
LFC (m)	553.18	574.87	1142.85

999

1000 TABLE 2. Base-state SBCAPE (J kg^{-1}) and MUCAPE (J kg^{-1}) at the plateau base (360–800 km)
1001 for the experiments with a MABL, with depths of 500 m, 1000 m, and 1500 m and potential
1002 temperature perturbations (θ') of -2 K, -3 K, -4 K, and -5 K relative to the base-state. All values
1003 are from single-point locations.

	500 m		1000 m		1500 m	
	SBCAPE	MUCAPE	SBCAPE	MUCAPE	SBCAPE	MUCAPE
	(J kg^{-1})					
-2 K	1350.95	1544.97	1182.24	1414.97	1196.59	1227.97
-3 K	1255.76	1544.97	1093.13	1414.97	1017.14	1046.87
-4 K	1163.53	1544.97	1006.98	1414.97	613.74	916.85
-5 K	1074.28	1544.97	923.83	1414.97	545.06	916.85

1004
1005
1006

1007

1008

1009

1010

1011

1012

1013

1014

1015

1016

1017
1018
1019
1020
1021
1022
1023

1024
1025
1026
1027
1028
1029
1030
1031
1032
1033
1034
1035

TABLE 3. Statistics of the MABL parcels released when the cold pools collide with the coldest MABLs ($-5\text{-K } \theta'$) with varied depths (indicated by the black contours in Figs. 10a–c), including buoyancy (B , 10^{-2} m s^{-2}), convective available potential energy (CAPE; J kg^{-1}), and convective inhibition (CIN; J kg^{-1}) at the release times (112 min, 109 min, and 107 min for 500-m, 1000-m, and 1500-m deep, respectively), parcel height (z_{10} , km) and vertical velocity (w , m s^{-1}) 10 min after release. Results are averaged over all MABL air parcels with $B < -0.01 \text{ m s}^{-2}$.

Experiment	B (10^{-2} m s^{-2})	CAPE (J kg^{-1})	CIN (J kg^{-1})	z_{10} (km)	w (m s^{-1})
500m_–5K	–4.45	1052.54	23.68	2.65	2.65
1000m_–5K	–5.16	705.38	19.25	3.26	3.42
1500m_–5K	–5.96	455.22	18.86	3.71	4.23

1036

1037 TABLE 4. Statistics of the MABL parcels released when the squall lines are at the plateau base
1038 (indicated by the black contours in Figs. 10d–f), including buoyancy (B , 10^{-2} m s^{-2}), CAPE (J
1039 kg^{-1}), and CIN (J kg^{-1}) at the release time (170 min for all experiments), parcel height (z_{20} , km)
1040 and vertical velocity (w , m s^{-1}) 20 min after release. Results are averaged over all MABL parcels
1041 with B of $[-0.1, -0.01] \text{ m s}^{-2}$. Note that the MABL parcels with $B < -0.1 \text{ m s}^{-2}$ are not included in
1042 the statistics to evaluate only parcels that are lifted to the updrafts (Figs. 11d–f).

Experiment	B (10^{-2} m s^{-2})	CAPE (J kg^{-1})	CIN (J kg^{-1})	z_{20} (km)	w (m s^{-1})
500m_–5K	–3.75	912.91	8.51	6.21	4.51
1000m_–5K	–4.89	685.52	13.61	5.66	4.03
1500m_–5K	–6.16	196.74	32.78	5.16	3.34

1043

1044

1045

1046

1047

1048

1049

1050

1051

1052

1053

1054

1055
 1056
 1057
 1058
 1059
 1060
 1061
 1062
 1063
 1064
 1065
 1066
 1067
 1068
 1069
 1070
 1071
 1072

TABLE 5. Positive vertical acceleration (dw/dt^+ , 10^{-2} m s $^{-2}$), its buoyant component (a_b^+ , 10^{-2} m s $^{-2}$), and inertial component (a_i^+ , 10^{-2} m s $^{-2}$); negative vertical acceleration (dw/dt^- , 10^{-2} m s $^{-2}$), its buoyant component (a_b^- , 10^{-2} m s $^{-2}$), and inertial component (a_i^- , 10^{-2} m s $^{-2}$). Positive (negative) vertical acceleration is a 10-min average after the collision time, for values $\geq 1 \times 10^{-2}$ m s $^{-2}$ ($\leq -1 \times 10^{-2}$ m s $^{-2}$) in an 8-km (horizontal) \times 5-km (vertical) domain centered on the CPLE (see Figs. 12 and 13 for reference).

Experiment	a_b^+ (10^{-2} m s $^{-2}$)	a_i^+ (10^{-2} m s $^{-2}$)	dw/dt^+ (10^{-2} m s $^{-2}$)	a_b^- (10^{-2} m s $^{-2}$)	a_i^- (10^{-2} m s $^{-2}$)	dw/dt^- (10^{-2} m s $^{-2}$)
CTRL	0.32	3.15	3.47	-0.29	-2.96	-3.25
500m_-5K	0.35	3.15	3.50	-0.32	-2.77	-3.09
1000m_-5K	0.32	3.11	3.43	-0.69	-2.49	-3.18
1500m_-5K	0.30	3.79	4.09	-0.75	-1.36	-2.11

1073
 1074
 1075
 1076
 1077
 1078
 1079
 1080
 1081
 1082
 1083
 1084
 1085
 1086
 1087
 1088
 1089
 1090
 1091
 1092

TABLE 6. Vorticity budget analysis following Rotunno et al. (1988), where C^2 ($\text{m}^2 \text{s}^{-2}$) is the net baroclinic generation of vorticity calculated from $C^2_L - C^2_R$; C^2_L and C^2_R are the baroclinically generated vorticity to the left and right of the CPLE; Δu^2_L are contributions from flows within the cold pool; C_J (m s^{-1}) represents the negative vorticity within the cold pool, including contributions from C^2 and Δu^2_L (Δu^2_L , $\text{m}^2 \text{s}^{-2}$); Δu_R (m s^{-1}) is the ambient wind shear east of the CPLE; $C_J/\Delta u$ is the balance approximation. Values of C^2_L and Δu^2_L (C^2_R and Δu_R) are averaged over 10 km west (east) of the CPLE from the terrain height ($z = 0.75$ km) to the top of cold pool ($z = 2.25$ km) when the cold pool collides with the upslope flow/moving MABL (107–113 min) on the slope, for the CTRL storm and the those encountering a 500-m deep $-5\text{-K } \theta'$, 1000-m deep $-5\text{-K } \theta'$ MABL, 1500-m deep $-5\text{-K } \theta'$ MABL.

	C^2_L ($\text{m}^2 \text{s}^{-2}$)	C^2_R ($\text{m}^2 \text{s}^{-2}$)	C^2 ($\text{m}^2 \text{s}^{-2}$)	Δu^2_L ($\text{m}^2 \text{s}^{-2}$)	C_J (m s^{-1})	Δu_R (m s^{-1})	$C_J/\Delta u_R$
CTRL	86.33	-32.41	118.74	315.77	20.84	11.76	1.77
MABL_500m_-5K	102.53	-23.82	126.35	345.59	21.72	12.24	1.77
MABL_1000m_-5K	99.11	22.15	76.96	215.50	17.10	14.30	1.20
MABL_1500m_-5K	117.30	64.54	52.76	269.29	17.95	15.30	1.17

1093
 1094
 1095
 1096
 1097
 1098
 1099
 1100
 1101
 1102
 1103
 1104
 1105
 1106
 1107
 1108
 1109
 1110
 1111
 1112

TABLE 7. Same as Table 6, but at 160–170 min when the cold pool arrives at the plateau base, for the CTRL storm and the those encountering a 500-m deep $-5\text{-K } \theta'$, 1500-m deep $-3\text{-K } \theta'$ MABL, 1500-m deep $-5\text{-K } \theta'$ MABL. For the experiment with 1500-m deep $-5\text{-K } \theta'$ MABL, results are calculated from $z = 0.5\text{--}2.25$ km due to the presence of an elevated cold pool.

	C^2_L ($\text{m}^2 \text{s}^{-2}$)	C^2_R ($\text{m}^2 \text{s}^{-2}$)	C^2 ($\text{m}^2 \text{s}^{-2}$)	Δu^2_L ($\text{m}^2 \text{s}^{-2}$)	C_J (m s^{-1})	Δu_R (m s^{-1})	$C_J/\Delta u_R$
CTRL	290.58	-7.03	297.61	30.80	18.12	11.10	1.63
MABL_500m_-5K	359.61	164.10	195.51	-7.27	13.72	10.06	1.36
MABL_1500m_-3K	318.59	159.98	158.61	41.09	14.13	14.42	0.98
MABL_1500m_-5K	210.18	160.93	49.25	33.76	9.11	9.83	0.93

1113

1114 **LIST OF FIGURES**

1115 FIG. 1. (a) Skew- T log- p diagram of the analytic sounding used for the numerical experiments,
 1116 with temperature ($^{\circ}\text{C}$, red line), mixing ratio (g kg^{-1} , blue line), and wind barbs. The dashed lines
 1117 represent the levels that are below the ground on the plateau top ($x = 0\text{--}300$ km). (b) Vertical
 1118 profiles of equivalent potential temperature (θ_e , K) at the base of the plateau ($x = 360\text{--}800$ km) for
 1119 the CTRL experiment (black solid line) and the MABL experiments (solid lines, dashed lines,
 1120 dash-dotted lines, and dotted lines represent MABLs with θ' values of -2 K, -3 K, -4 K, and -5
 1121 K, respectively; orange, magenta, and blue lines represent MABLs with depths of 500 m, 1000 m,
 1122 and 1500 m, respectively). 55

1123

1124 FIG. 2. Precipitation mixing ratio (g kg^{-1} , including rain, snow, and graupel, shaded), cloud mixing
 1125 ratio (black contours of 0.5 g kg^{-1} , including cloud water and cloud ice), and u - w wind (reference
 1126 vector of 10 m s^{-1}) at 60 min, 120 min, 180 min, and 240 min for simulations including (a1–a4) a
 1127 1.5-km plateau (CTRL), (b1–b4) no terrain (NoTER), (c1–c4) a 1.5-km elevated surface across
 1128 the full domain (OnlyTER). Terrain is shaded gray. 56

1129

1130 FIG. 3. Hovmöller diagrams of total column precipitation mass (kg m^{-2} , including rain, snow, and
 1131 graupel mass, shaded) vertically integrated from the ground to 10 km height above ground level
 1132 (AGL) for simulations including (a) a 1.5 km plateau (CTRL), (b) no terrain (NoTER), and (c) a
 1133 1.5-km elevated surface across the full domain (OnlyTER). Grey dashed lines bracket the
 1134 horizontal range of the plateau slope ($x = 300\text{--}360$ km). 57

1135

1136 FIG. 4. Time series of domain total precipitation mass (10^7 kg) summed from 0–10 km AGL for
 1137 the control experiment (CTRL; black solid line) and the MABL experiments (solid lines, dashed
 1138 lines, dash-dotted lines, and dotted lines represent MABLs with θ' values of -2 K, -3 K, -4 K,
 1139 and -5 K, respectively; orange, magenta, and blue lines represent MABLs with depths of 500 m,
 1140 1000 m, and 1500 m, respectively). Vertical black dashed lines divide the storm evolution into
 1141 three phases: (0–90 min) over the plateau top, (90–150 min) over the slope, and (150–480 min) at

1142 the plateau bottom..... 58

1143

1144 FIG. 5. Time series from 100–150 min of (a) 0–3 km AGL maximum vertical velocity (w_{\max} , m

1145 s^{-1}), (b) 0–8 km AGL total precipitation mass (10^7 kg), and (c) rain rate ($mm\ h^{-1}$). Results are a

1146 10-km average from 7 km behind to 3 km in front of the cold pool leading edge (CPLE). The initial

1147 cold pool-MABL (cold pool-upslope flow for the CTRL) collision times (ranging between 107–

1148 113 min for different experiments) are highlighted by a red solid bar. Solid lines, dashed lines,

1149 dash-dotted lines, and dotted lines represent MABLs with θ' values of -2 K, -3 K, -4 K, and -5

1150 K, respectively; orange, magenta, and blue lines represent MABLs with depths of 500 m, 1000 m,

1151 and 1500m, respectively. 59

1152

1153 FIG. 6. Upslope wind speed [$m\ s^{-1}$, shaded, positive (negative) values are defined as wind in the

1154 upslope (downslope) direction] and u - w wind vectors (reference vector of $4\ m\ s^{-1}$) at 100 min for

1155 (a) the CTRL experiment, and experiments with a -5 -K θ' (b) 500-m deep, (c) 1000-m deep, (d)

1156 1500-m deep MABL. All experiments are conducted *in the absence of a squall line* to more clearly

1157 illustrate the development of the upslope flows. The magenta contour marks the $0\ m\ s^{-1}$ wind line.

1158 The frontal edge of the upslope winds is indicated by a black dashed line. Terrain is shaded gray.

1159 60

1160

1161 FIG. 7. CTRL storm total mixing ratio (q , $g\ kg^{-1}$, including cloud water, cloud ice, rain, snow, and

1162 graupel, shaded) and u - w wind (reference vector of $10\ m\ s^{-1}$) at (a1) 120 min, (a2) 180 min, and

1163 (a3) 300 min; (b1)–(b3) equivalent potential temperature (θ_e , K, shaded) and cloud water mixing

1164 ratio q_c (black contour of $0.5\ g\ kg^{-1}$); (c1)–(c3) buoyancy (B , $10^{-2}\ m\ s^{-2}$, shaded) and vertical

1165 velocity w ($4\ m\ s^{-1}$ contoured solid black; $8\ m\ s^{-1}$ contoured dashed black; $12\ m\ s^{-1}$ contoured

1166 solid cyan). The cold pool leading edge (CPLE) is indicated by the magenta dashed line. Note that

1167 the y -axis range differs in panels (a1)–(a3), (b1)–(b3), and (c1)–(c3)..... 61

1168

1169 FIG. 8. Same as Fig. 7, but for the experiment with a 1500-m deep, -5 -K θ' MABL. 62

1170

1171 FIG. 9. Same as Fig. 7, but for the experiment with a 1000-m deep, -5 -K θ' MABL. 63

1172
1173 FIG. 10. Same as Fig. 7, but for the experiment with a 500-m deep, $-5\text{-K } \theta'$ MABL. 64

1174
1175 FIG. 11. Trajectory centroids of MABL parcels (defined by buoyancy $< -0.01 \text{ m s}^{-2}$) released 4–
1176 6 km in front of the CPLE (area shown by black closed contour) (a–c) at the initial collision times
1177 between the cold pools and a $-5\text{-K } \theta'$ (a) 500-m deep, (b) 1000-m deep, (c) 1500-m deep MABL;
1178 (d–f) as in (a–c) but for parcels released at 170 min. Parcels with buoyancy between $[-0.04, -0.01)$
1179 m s^{-2} are contoured solid black, $[-0.07, -0.04) \text{ m s}^{-2}$ are dashed black, $[-0.10, -0.07) \text{ m s}^{-2}$ are
1180 dashed dotted black, and $< -0.10 \text{ m s}^{-2}$ are dotted black. Black circles indicate the selected parcels'
1181 centroid positions after 10 min (note the trajectory paths extend beyond 10 min). Vertical
1182 displacements (km) after 10 min for all parcels released in the full domain displayed in the figure
1183 panels are shaded. The MABL is contoured blue, defined by a buoyancy value of -0.01 m s^{-2} .
1184 Terrain is shaded gray. The x -axis is distance with respect to the CPLE. Storm motion is not
1185 removed from the parcel trajectories. 65

1186
1187 FIG. 12. CTRL storm 10-min averaged (from the collision time to 10 min after) (a) vertical
1188 acceleration dw/dt (10^{-1} m s^{-2} , shaded), inertial acceleration a_i (intervals of 0.02 m s^{-2} contoured
1189 black), buoyant acceleration a_b (intervals of 0.02 m s^{-2} contoured cyan), u - w wind (reference vector
1190 of 6 m s^{-1} , u wind is relative to the CPLE speed), and vertical velocity (8 m s^{-1} contoured magenta);
1191 (b) non-hydrostatic pressure perturbation p'_{nh} (hPa, shaded), inertial pressure perturbation $p'_{i(nh)}$
1192 (intervals of 0.3 hPa contoured black), and buoyant pressure perturbation $p'_{b(nh)}$ (intervals of 0.3
1193 hPa contoured cyan); (c) $p'_{i(nh)}$ (hPa, shaded) and a_i (intervals of 0.02 m s^{-2} contoured black); (d)
1194 the sum of the *splat* and *spin* terms (10^{-3} s^{-2} , shaded), and $p'_{i(nh)}$ (intervals of 0.2 hPa contoured
1195 black). Difference from 10 min before to 10 min after the collision time of (e) horizontal vorticity
1196 (10^{-2} s^{-1} , shaded) and u - w wind (reference vector of 4 m s^{-1}); (f) baroclinic term ($-\partial B/\partial x$, 10^{-4} s^{-2} ,
1197 shaded) and horizontal vorticity (intervals of $8 \times 10^{-3} \text{ s}^{-1}$ contoured black). All results are spatially
1198 averaged relative to the CPLE (gray dashed line). Positive (negative) values are indicated by solid
1199 (dotted) lines, and terrain is shaded gray. 67

1200
1201 FIG. 13. Vertical acceleration dw/dt (10^{-1} m s^{-2} , shaded), a_i (intervals of 0.02 m s^{-2} contoured

1202 black), a_b (intervals of 0.02 m s^{-2} contoured cyan), $u-w$ wind (reference vector of 6 m s^{-1} , u wind
 1203 is relative to the CPLE speed), and vertical velocity (8 m s^{-1} contoured magenta) for experiments
 1204 with a $-5\text{-K } \theta'$ (a) 500-m deep, (d) 1000-m deep, (g) 1500-m deep MABL. For the same three
 1205 MABL experiments, (b, e, h) $p'_{i(nh)}$ (hPa, shaded) and a_i (intervals of 0.02 m s^{-2} contoured black),
 1206 (c, f, i) the sum of *splat* and *spin* terms (10^{-3} s^{-2} , shaded) and $p'_{i(nh)}$ (intervals of 0.2 hPa contoured
 1207 black)..... 69

1208
 1209 FIG. 14. CTRL storm (a) buoyancy (B , 10^{-2} m s^{-2} , shaded), vertical velocity (w , 4 m s^{-1} contoured
 1210 solid black, 7 m s^{-1} contoured dotted black, 10 m s^{-1} contoured solid cyan), LFC (km, magenta
 1211 dashed line), and $u-w$ wind (\mathbf{V} , m s^{-1} , reference vector of 6 m s^{-1} , u wind is relative to the CPLE
 1212 speed) at (a1) 150 min, (a2) 160 min, and (a3) 170 min; (b) vertical acceleration dw/dt (10^{-1} m s^{-2} ,
 1213 shaded), inertial acceleration a_i (10^{-1} m s^{-2} , intervals of 0.02 m s^{-2} contoured black), buoyant
 1214 acceleration a_b (10^{-1} m s^{-2} , intervals of 0.02 m s^{-2} contoured cyan), and $u-w$ wind (reference vector
 1215 of 6 m s^{-1} , u wind is relative to the CPLE speed) at (b1) 150 min, (b2) 160 min, and (b3) 170 min;
 1216 (c) equivalent potential temperature θ_e (K, shaded), moisture flux vectors ($q\mathbf{V}$, reference vector of
 1217 $6 \times 10^{-2} \text{ kg m}^{-2} \text{ s}^{-1}$, horizontal component is relative to the CPLE speed), vertical moisture flux (5
 1218 $\times 10^{-2} \text{ kg m}^{-2} \text{ s}^{-1}$ contoured black), and cloud water mixing ratio (q_c , 1.2 g kg^{-1} contoured dashed
 1219 magenta) at (c1) 150 min, (c2) 160 min, and (c3) 170 min. All the results are averaged relative to
 1220 the CPLE (black dashed line) from each time (150 min, 160 min, and 170 min) to 10 min later.
 1221 Terrain is shaded gray..... 70

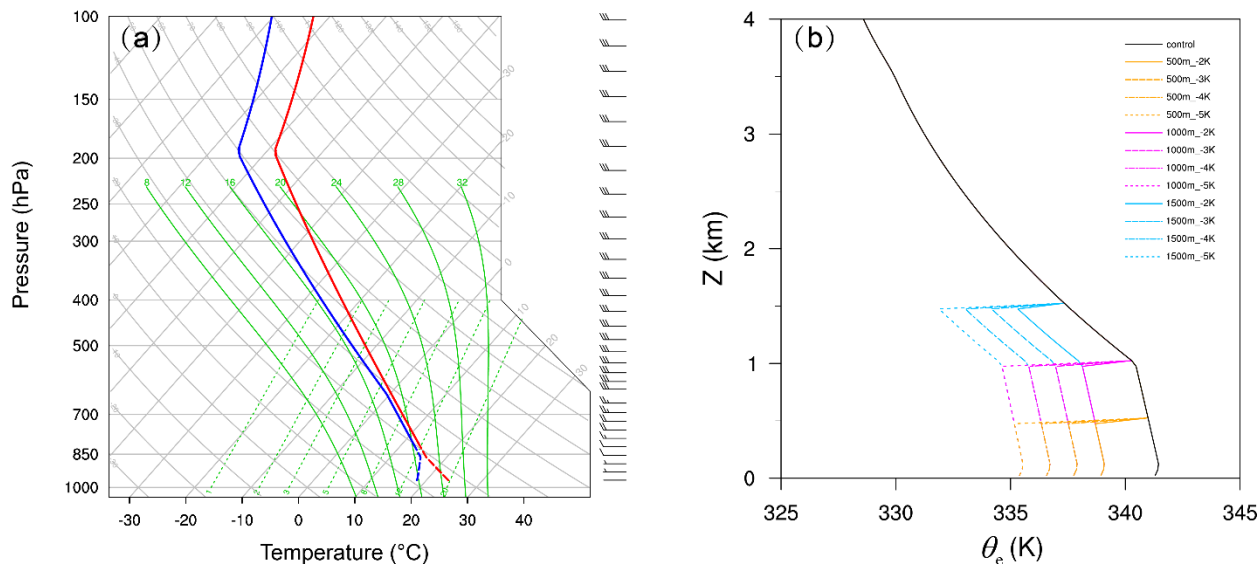
1222
 1223 FIG. 15. Same as Fig. 14, but for the experiment with a 1500-m deep, $-5\text{-K } \theta'$ MABL. 72

1224
 1225 FIG. 16. Same as Fig. 14, but for the experiment with a 500-m deep, $-5\text{-K } \theta'$ MABL. 73

1226
 1227 FIG. 17. Same as Fig. 14, but for the experiment with a 1500-m deep, $-3\text{-K } \theta'$ MABL. 74

1228
 1229 FIG. 18. Schematic diagram of a squall line descending a plateau slope and encountering an
 1230 upslope moving (a) 500-m deep, $-5\text{-K } \theta'$ MABL, where cold pool lifted air parcels are accelerated
 1231 downward due to a baroclinically-generated $p'_{i(nh)}$, (b) 1500-m deep, $-5\text{-K } \theta'$ MABL, where cold

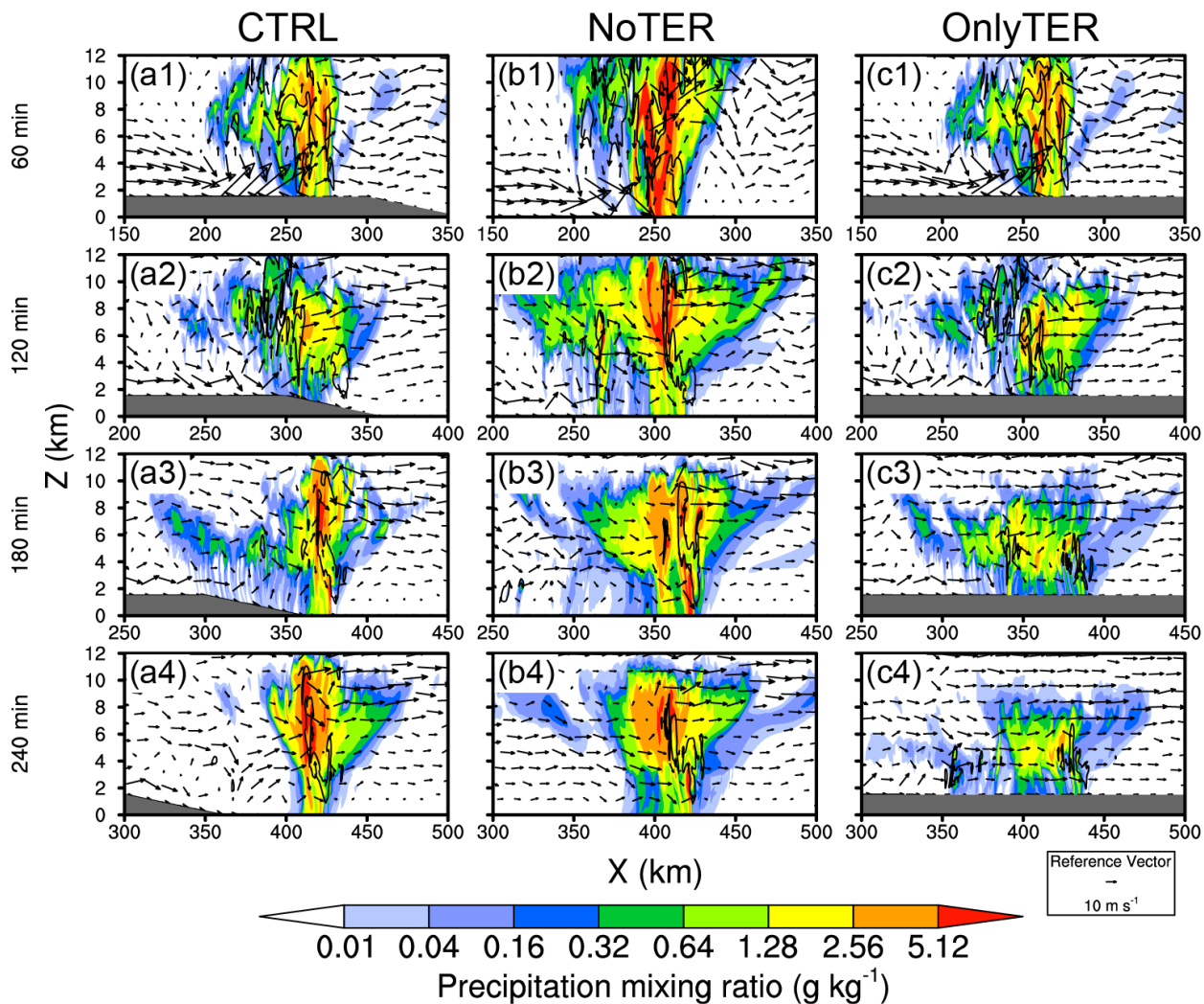
1232 pool lifted parcels rise unimpeded into the updraft due to the smaller, weaker $p'_{i(nh)}$. Squall lines
 1233 moving away from the terrain over a (c) 500-m deep, $-3\text{-K } \theta'$ MABL, where a surface-based cold
 1234 pool lifts low- θ_e air from within the MABL and an elevated bore lifts high- θ_e air from above the
 1235 MABL into the updraft, (d) 1500-m deep, $-5\text{-K } \theta'$ MABL, where only a thin layer of high- θ_e air
 1236 is available for bore-induced lift, with no surface-based cold pool ascent.
 123775



1238
 1239 FIG. 1. (a) Skew- T log- p diagram of the analytic sounding used for the numerical experiments,
 1240 with temperature ($^{\circ}\text{C}$, red line), mixing ratio (g kg^{-1} , blue line), and wind barbs. The dashed lines
 1241 represent the levels that are below the ground on the plateau top ($x = 0\text{--}300$ km). (b) Vertical
 1242 profiles of equivalent potential temperature (θ_e , K) at the base of the plateau ($x = 360\text{--}800$ km) for
 1243 the CTRL experiment (black solid line) and the MABL experiments (solid lines, dashed lines,
 1244 dash-dotted lines, and dotted lines represent MABLs with θ' values of -2 K, -3 K, -4 K, and -5
 1245 K, respectively; orange, magenta, and blue lines represent MABLs with depths of 500 m, 1000 m,
 1246 and 1500 m, respectively).

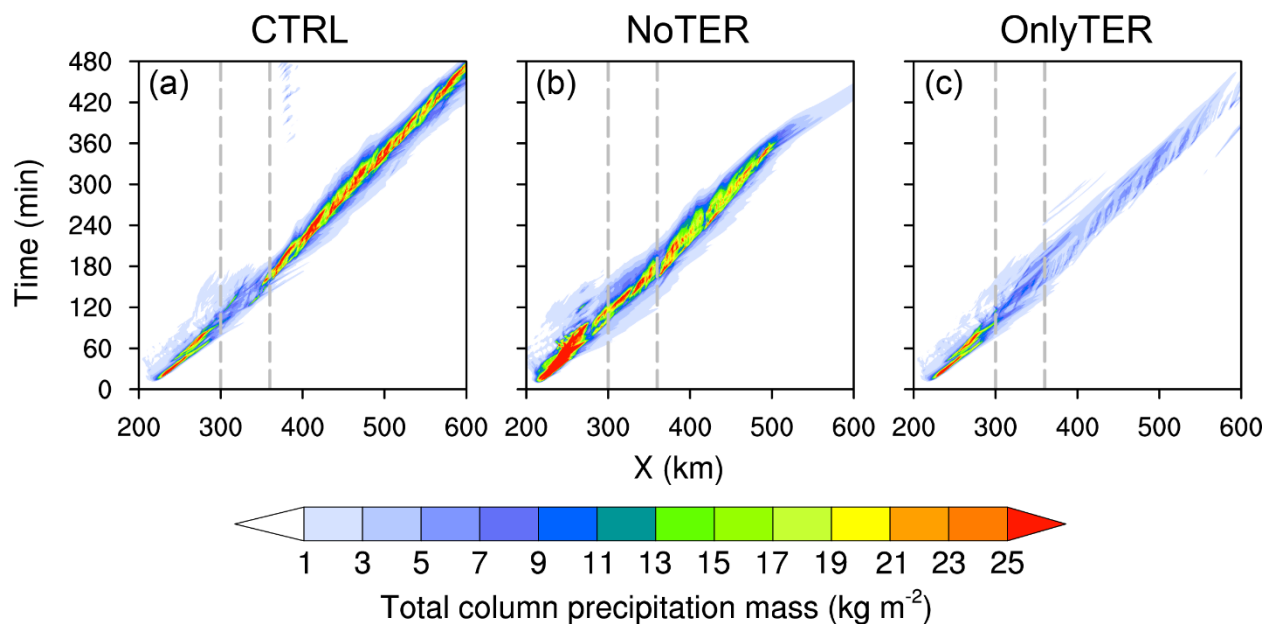
1247
 1248

1249
1250
1251
1252
1253



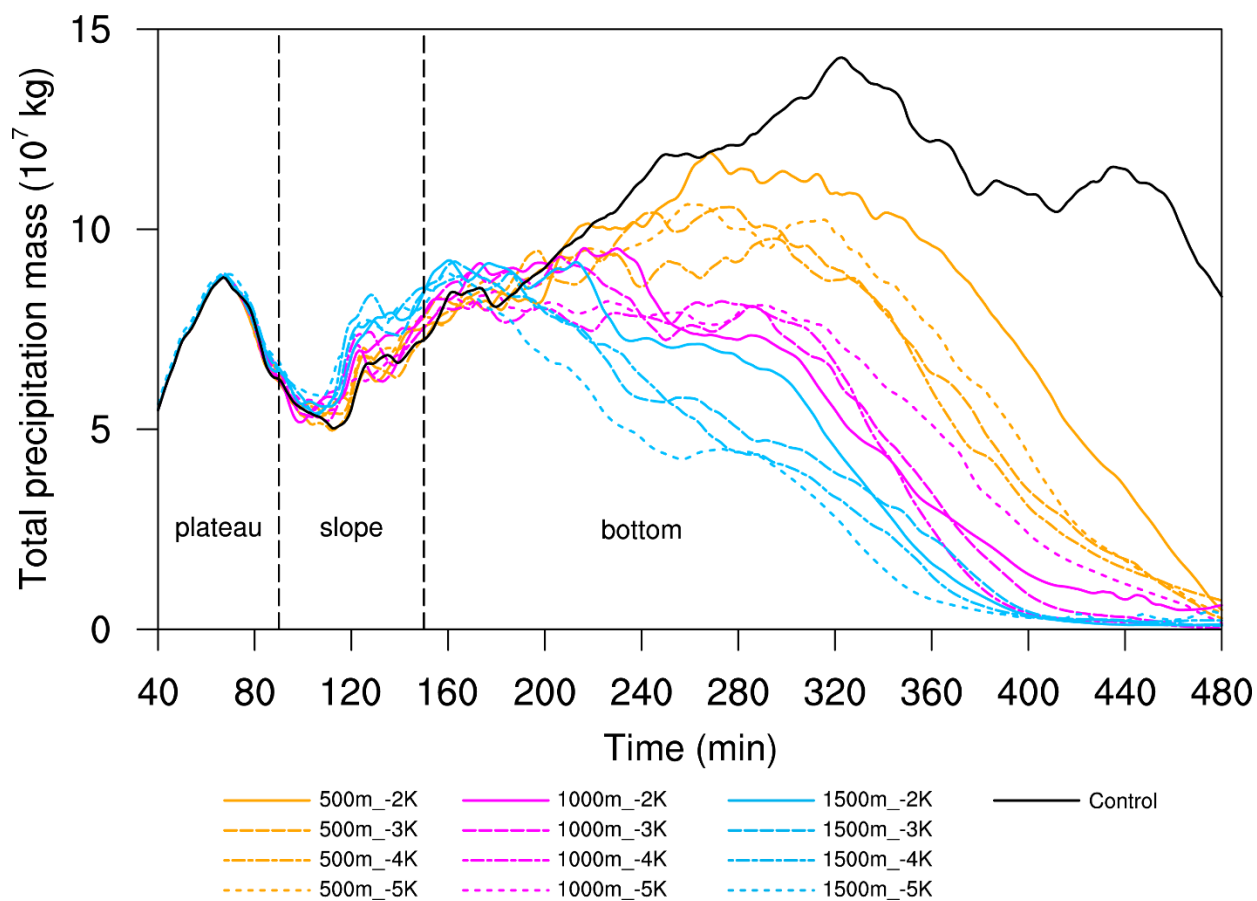
1254
1255 FIG. 2. Precipitation mixing ratio (g kg^{-1} , including rain, snow, and graupel, shaded), cloud mixing
1256 ratio (black contours of 0.5 g kg^{-1} , including cloud water and cloud ice), and $u-w$ wind (reference
1257 vector of 10 m s^{-1}) at 60 min, 120 min, 180 min, and 240 min for simulations including (a1–a4) a
1258 1.5-km plateau (CTRL), (b1–b4) no terrain (NoTER), (c1–c4) a 1.5-km elevated surface across

1259 the full domain (OnlyTER). Terrain is shaded gray.



1260
1261 FIG. 3. Hovmöller diagrams of total column precipitation mass (kg m^{-2} , including rain, snow, and
1262 graupel mass, shaded) vertically integrated from the ground to 10 km height above ground level
1263 (AGL) for simulations including (a) a 1.5 km plateau (CTRL), (b) no terrain (NoTER), and (c) a
1264 1.5-km elevated surface across the full domain (OnlyTER). Grey dashed lines bracket the
1265 horizontal range of the plateau slope ($x = 300\text{--}360$ km).

1266
1267
1268
1269
1270
1271
1272
1273



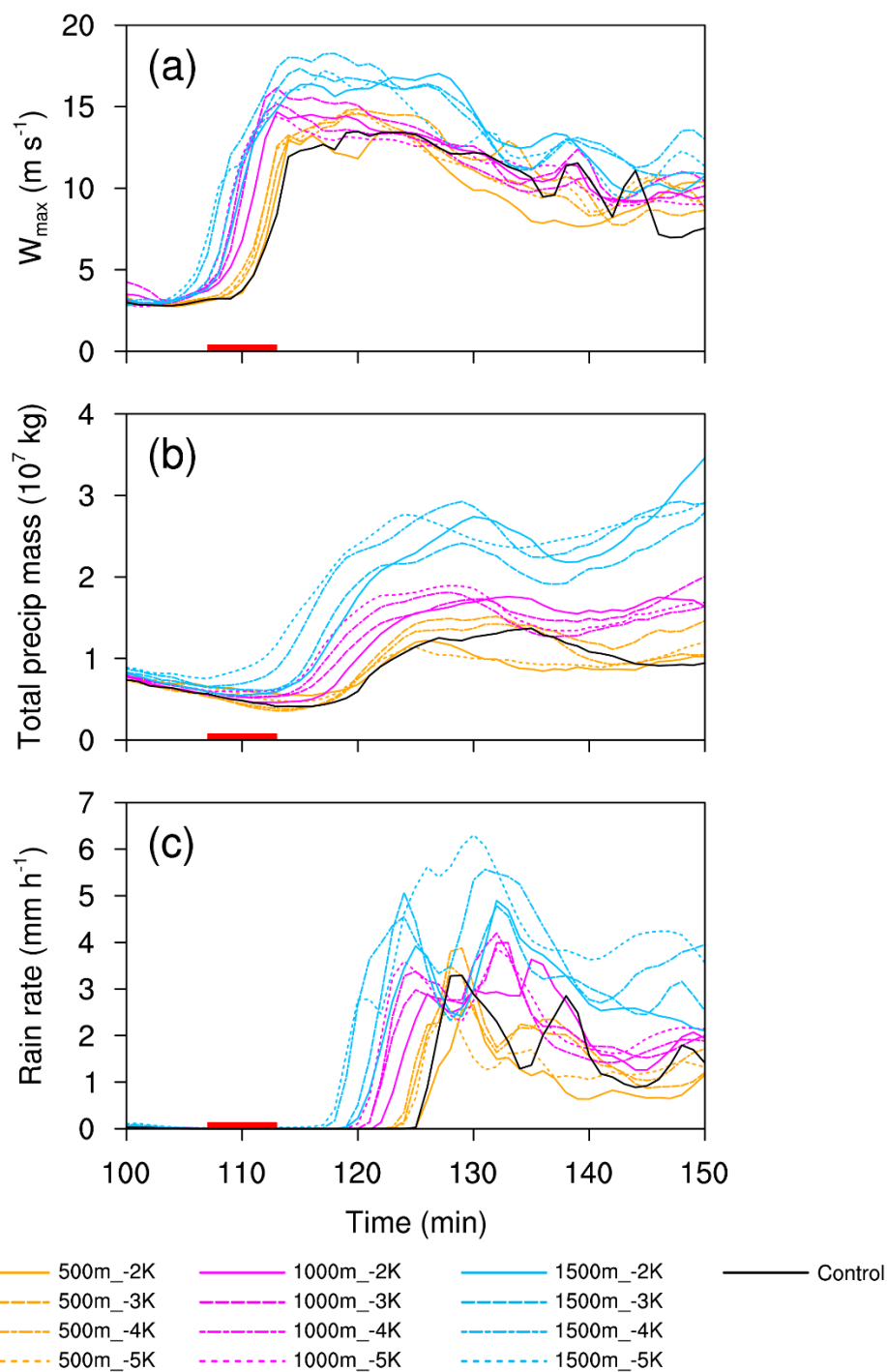
1275

1276 FIG. 4. Time series of domain total precipitation mass (10^7 kg) summed from 0–10 km AGL for
 1277 the control experiment (CTRL; black solid line) and the MABL experiments (solid lines, dashed
 1278 lines, dash-dotted lines, and dotted lines represent MABLs with θ' values of -2 K, -3 K, -4 K,
 1279 and -5 K, respectively; orange, magenta, and blue lines represent MABLs with depths of 500 m,
 1280 1000 m, and 1500 m, respectively). Vertical black dashed lines divide the storm evolution into
 1281 three phases: (0–90 min) over the plateau top, (90–150 min) over the slope, and (150–480 min) at
 1282 the plateau bottom.

1283

1284

1285



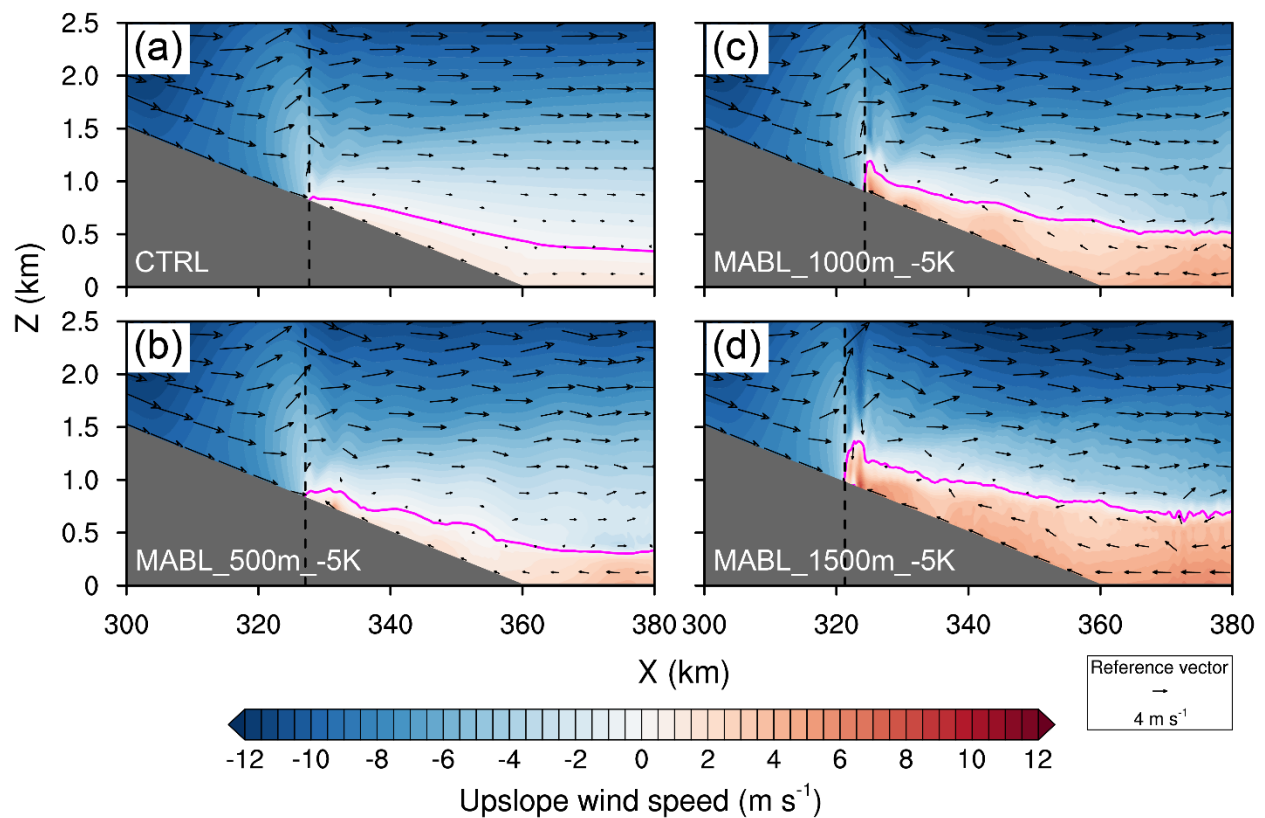
1287

1288 FIG. 5. Time series from 100–150 min of (a) 0–3 km AGL maximum vertical velocity (w_{\max} , m
 1289 s^{-1}), (b) 0–8 km AGL total precipitation mass (10^7 kg), and (c) rain rate (mm h^{-1}). Results are a
 1290 10-km average from 7 km behind to 3 km in front of the cold pool leading edge (CPL). The initial

1291 cold pool-MABL (cold pool-upslope flow for the CTRL) collision times (ranging between 107–
 1292 113 min for different experiments) are highlighted by a red solid bar. Solid lines, dashed lines,
 1293 dash-dotted lines, and dotted lines represent MABLs with θ' values of -2 K, -3 K, -4 K, and -5
 1294 K, respectively; orange, magenta, and blue lines represent MABLs with depths of 500 m, 1000 m,
 1295 and 1500m, respectively.

1296

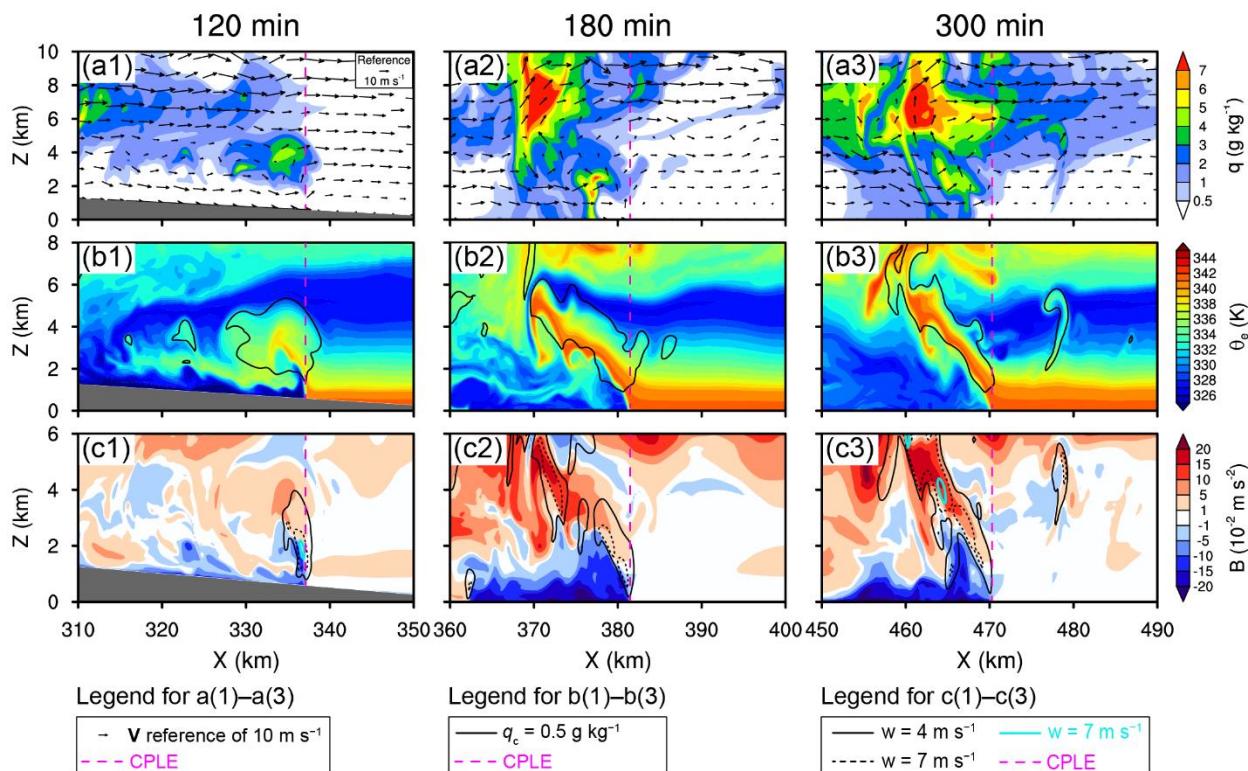
1297



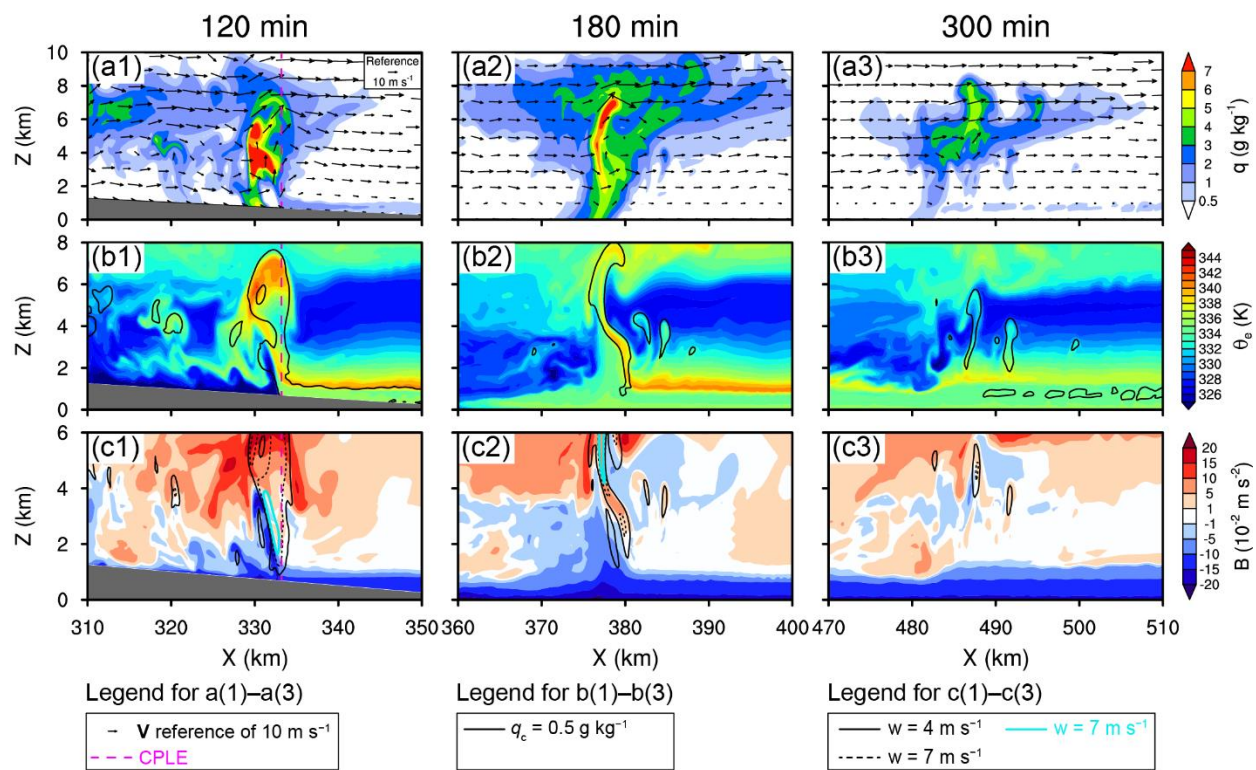
1298

1299 FIG. 6. Upslope wind speed [m s^{-1} , shaded, positive (negative) values are defined as wind in the
 1300 upslope (downslope) direction] and $u-w$ wind vectors (reference vector of 4 m s^{-1}) at 100 min for
 1301 (a) the CTRL experiment, and experiments with a -5-K θ' (b) 500-m deep, (c) 1000-m deep, (d)
 1302 1500-m deep MABL. All experiments are conducted *in the absence of a squall line* to more clearly

1303 illustrate the development of the upslope flows. The magenta contour marks the 0 m s^{-1} wind line.
 1304 The frontal edge of the upslope winds is indicated by a black dashed line. Terrain is shaded gray.
 1305



1306
 1307 FIG. 7. CTRL storm total mixing ratio (q , g kg^{-1} , including cloud water, cloud ice, rain, snow, and
 1308 graupel, shaded) and u - w wind (reference vector of 10 m s^{-1}) at (a1) 120 min, (a2) 180 min, and
 1309 (a3) 300 min; (b1)–(b3) equivalent potential temperature (θ_e , K, shaded) and cloud water mixing
 1310 ratio q_c (black contour of 0.5 g kg^{-1}); (c1)–(c3) buoyancy (B , 10^{-2} m s^{-2} , shaded) and vertical
 1311 velocity w (4 m s^{-1} contoured solid black; 8 m s^{-1} contoured dashed black; 12 m s^{-1} contoured
 1312 solid cyan). The cold pool leading edge (CPLE) is indicated by the magenta dashed line. Note that
 1313 the y -axis range differs in panels (a1)–(a3), (b1)–(b3), and (c1)–(c3).

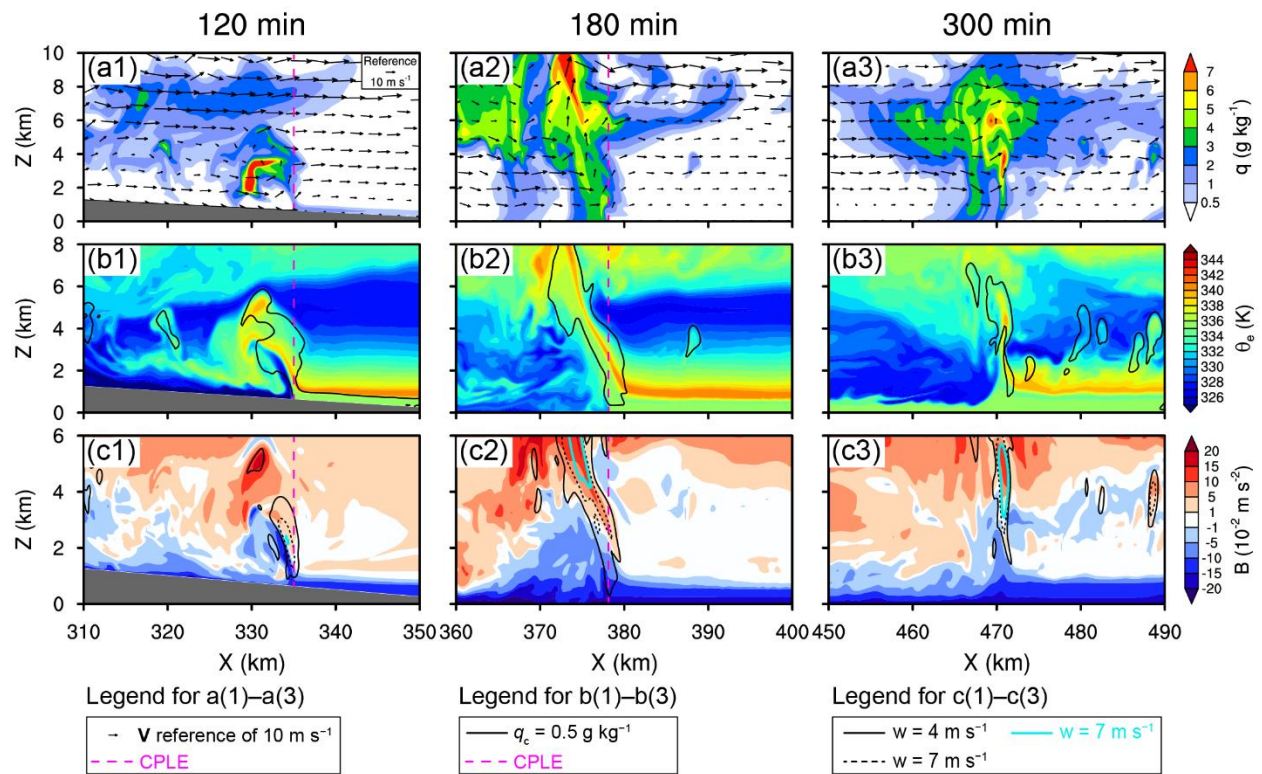


1314

1315 FIG. 8. Same as Fig. 7, but for the experiment with a 1500-m deep, $-5\text{-K } \theta'$ MABL.

1316

1317



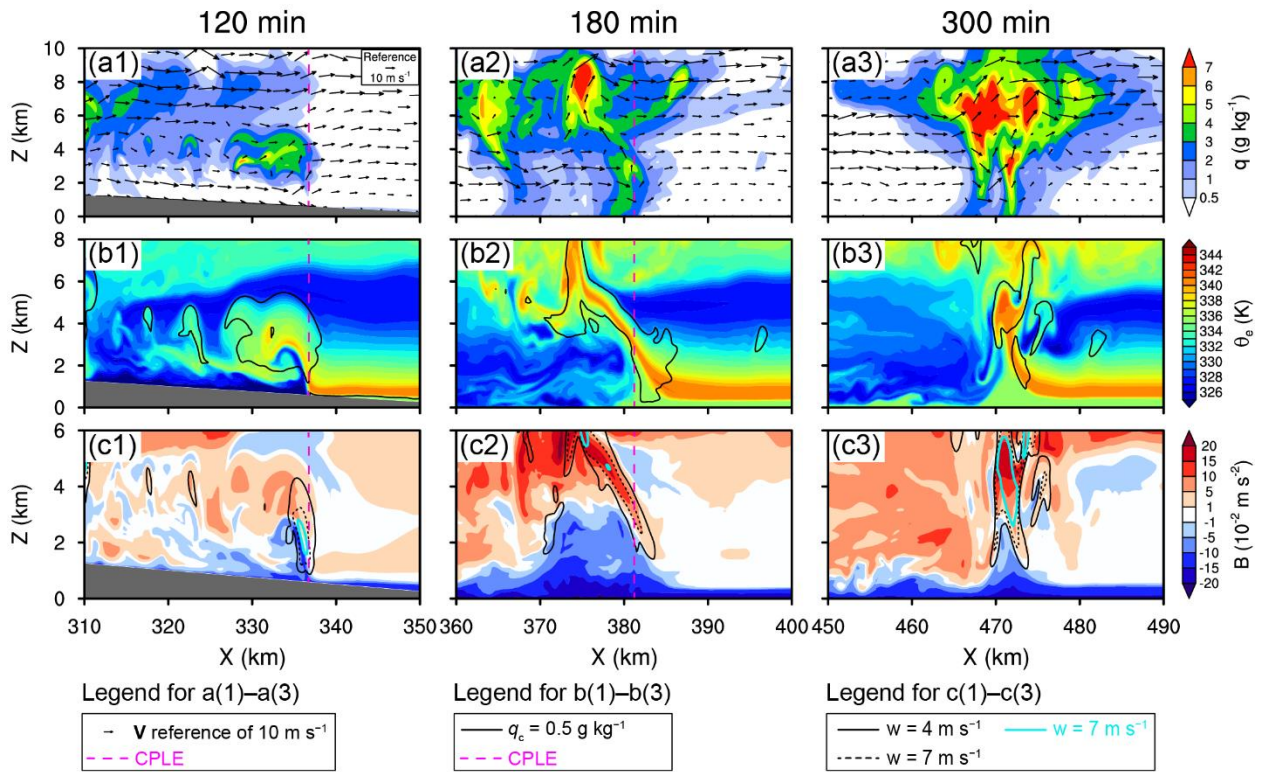
1318

1319 FIG. 9. Same as Fig. 7, but for the experiment with a 1000-m deep, -5 -K θ' MABL.

1320

1321

1322



1323

1324 FIG. 10. Same as Fig. 7, but for the experiment with a 500-m deep, $-5\text{-K } \theta'$ MABL.

1325

1326

1327

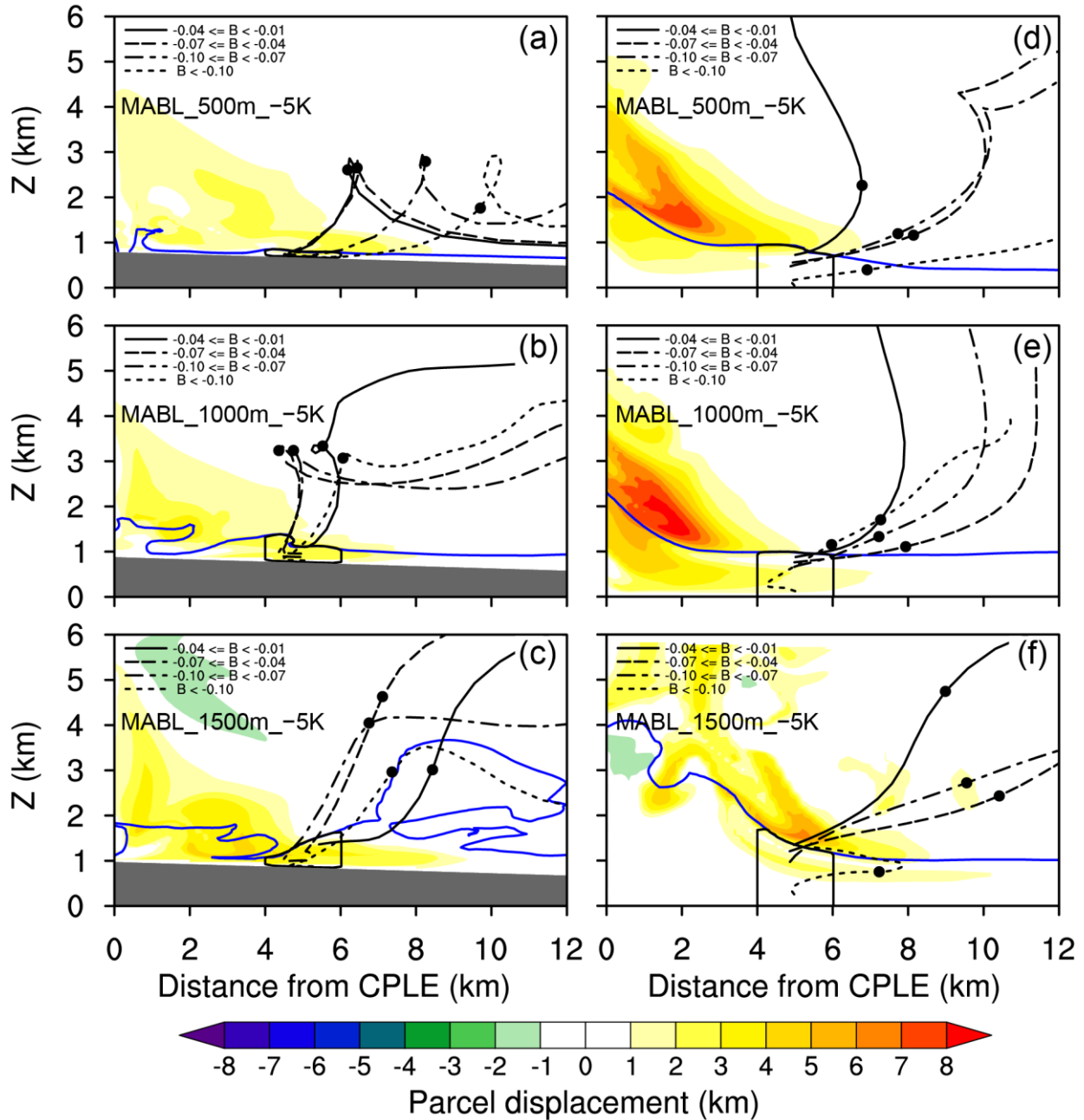
1328

1329

1330

1331

1332



1333

1334 FIG. 11. Trajectory centroids of MABL parcels (defined by buoyancy $< -0.01 \text{ m s}^{-2}$) released 4–6

1335 km in front of the CPLE (area shown by black closed contour) (a–c) at the initial collision times

1336 between the cold pools and a $-5\text{-K } \theta'$ (a) 500-m deep, (b) 1000-m deep, (c) 1500-m deep MABL;

1337 (d–f) as in (a–c) but for parcels released at 170 min. Parcels with buoyancy between $[-0.04, -0.01)$

1338 m s^{-2} are contoured solid black, $[-0.07, -0.04) \text{ m s}^{-2}$ are

1339 dashed dotted black, and $< -0.10 \text{ m s}^{-2}$ are dotted black. Black circles indicate the selected parcels'
1340 centroid positions after 10 min (note the trajectory paths extend beyond 10 min). Vertical
1341 displacements (km) after 10 min for all parcels released in the full domain displayed in the figure
1342 panels are shaded. The MABL is contoured blue, defined by a buoyancy value of -0.01 m s^{-2} .
1343 Terrain is shaded gray. The x -axis is distance with respect to the CPLE. Storm motion is not
1344 removed from the parcel trajectories.

1345

1346

1347

1348

1349

1350

1351

1352

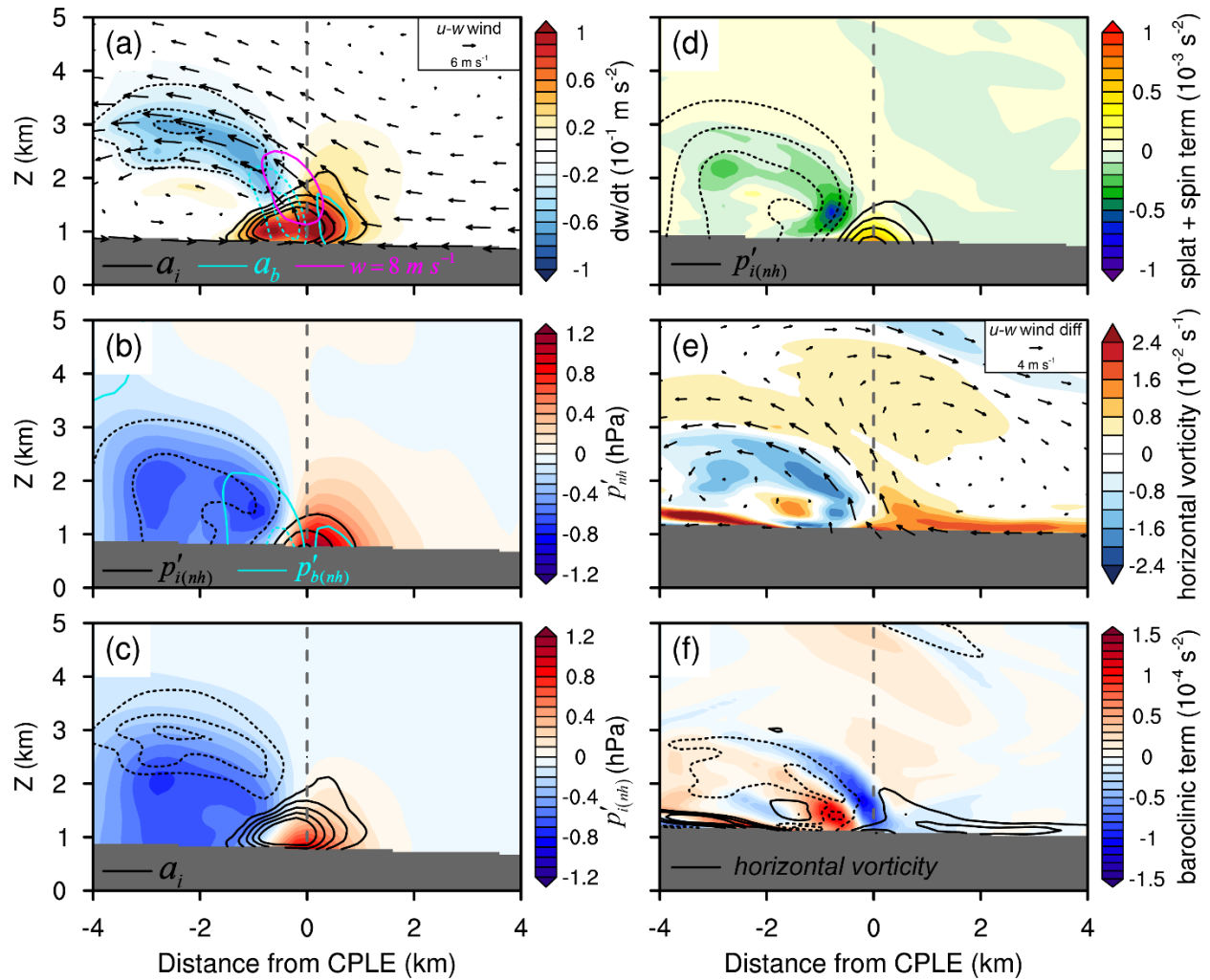
1353

1354

1355

1356

1357



1358

1359 FIG. 12. CTRL storm 10-min averaged (from the collision time to 10 min after) (a) vertical
 1360 acceleration dw/dt ($10^{-1} m s^{-2}$, shaded), inertial acceleration a_i (intervals of $0.02 m s^{-2}$ contoured
 1361 black), buoyant acceleration a_b (intervals of $0.02 m s^{-2}$ contoured cyan), $u-w$ wind (reference
 1362 vector of $6 m s^{-1}$, u wind is relative to the CPLE speed), and vertical velocity ($8 m s^{-1}$ contoured
 1363 magenta); (b) non-hydrostatic pressure perturbation p'_{nh} (hPa, shaded), inertial pressure
 1364 perturbation $p'_{i(nh)}$ (intervals of $0.3 hPa$ contoured black), and buoyant pressure perturbation $p'_{b(nh)}$
 1365 (intervals of $0.3 hPa$ contoured cyan); (c) $p'_{i(nh)}$ (hPa, shaded) and a_i (intervals of $0.02 m s^{-2}$
 1366 contoured black); (d) the sum of the *splat* and *spin* terms ($10^{-3} s^{-2}$, shaded), and $p'_{i(nh)}$ (intervals of
 1367 $0.2 hPa$ contoured black). Difference from 10 min before to 10 min after the collision time of (e)

1368 horizontal vorticity (10^{-2} s^{-1} , shaded) and u - w wind (reference vector of 4 m s^{-1}); (f) baroclinic
1369 term ($-\partial B/\partial x$, 10^{-4} s^{-2} , shaded) and horizontal vorticity (intervals of $8 \times 10^{-3} \text{ s}^{-1}$ contoured black).
1370 All results are spatially averaged relative to the CPLE (gray dashed line). Positive (negative) values
1371 are indicated by solid (dotted) lines, and terrain is shaded gray.

1372

1373

1374

1375

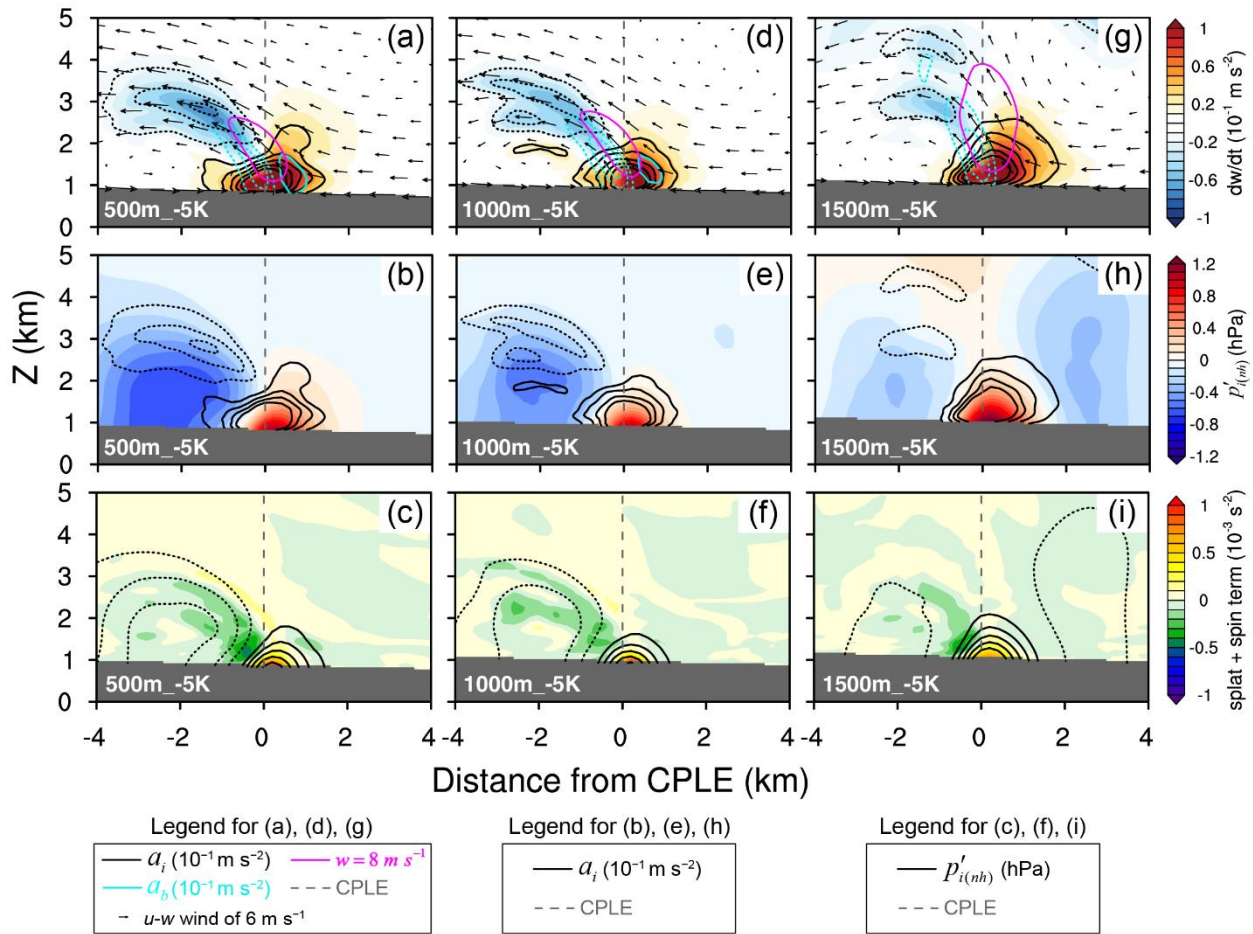
1376

1377

1378

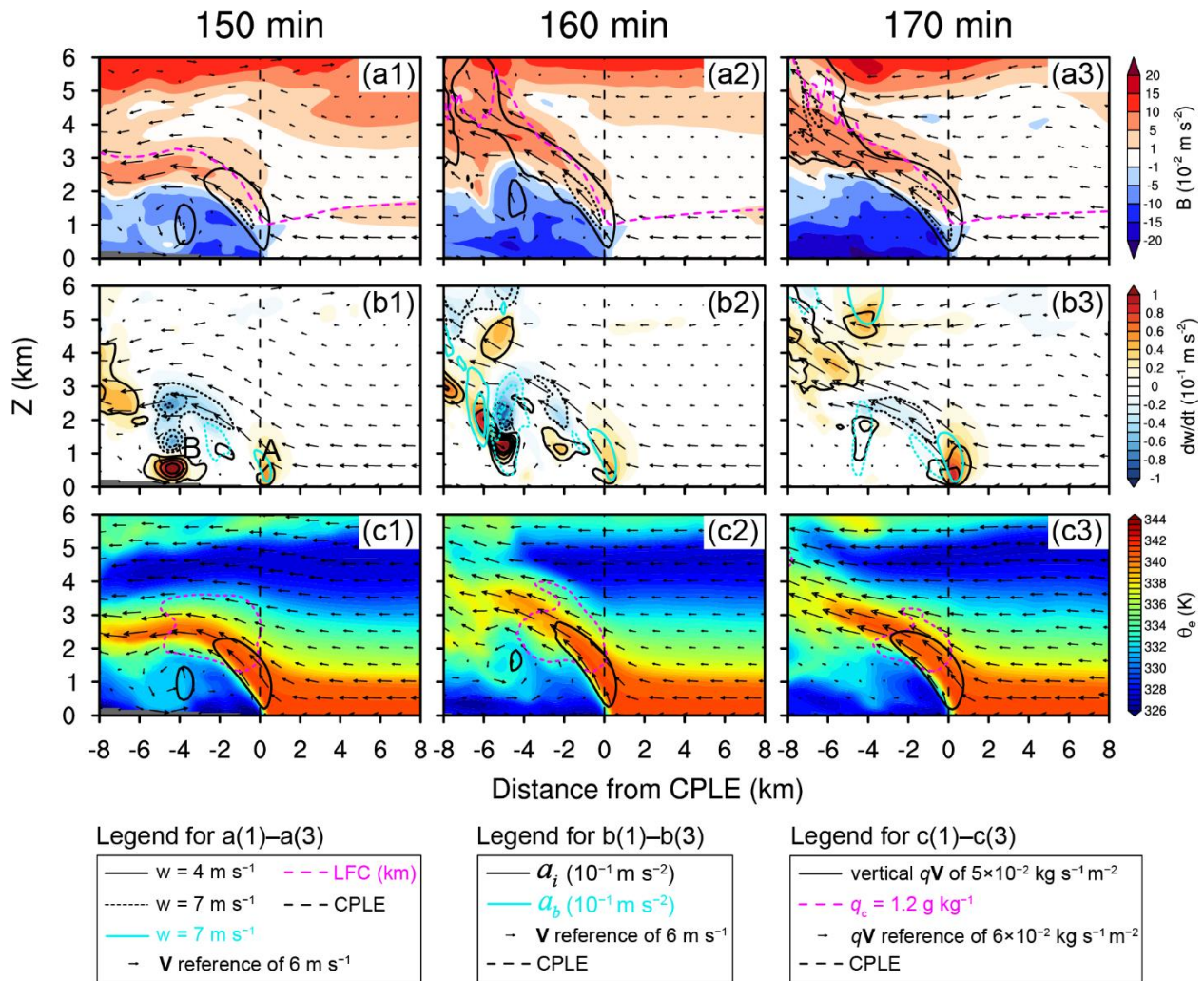
1379

1380



1381
 1382 FIG. 13. Vertical acceleration dw/dt (10^{-1} m s^{-2} , shaded), a_i (intervals of 0.02 m s^{-2} contoured
 1383 black), a_b (intervals of 0.02 m s^{-2} contoured cyan), $u-w$ wind (reference vector of 6 m s^{-1} , u wind
 1384 is relative to the CPLE speed), and vertical velocity (8 m s^{-1} contoured magenta) for experiments
 1385 with a $-5\text{-K } \theta'$ (a) 500-m deep, (d) 1000-m deep, (g) 1500-m deep MABL. For the same three
 1386 MABL experiments, (b, e, h) $p'_{i(nh)}$ (hPa, shaded) and a_i (intervals of 0.02 m s^{-2} contoured black),
 1387 (c, f, i) the sum of *splat* and *spin* terms (10^{-3} s^{-2} , shaded) and $p'_{i(nh)}$ (intervals of 0.2 hPa contoured
 1388 black).

1389
 1390
 1391



1392

1393 FIG. 14. CTRL storm (a) buoyancy (B , 10^{-2} m s^{-2} , shaded), vertical velocity (w , 4 m s^{-1} contoured
 1394 solid black, 7 m s^{-1} contoured dotted black, 10 m s^{-1} contoured solid cyan), LFC (km, magenta
 1395 dashed line), and u - w wind (\mathbf{V} , m s^{-1} , reference vector of 6 m s^{-1} , u wind is relative to the CPLE
 1396 speed) at (a1) 150 min, (a2) 160 min, and (a3) 170 min; (b) vertical acceleration dw/dt (10^{-1} m s^{-2} ,
 1397 shaded), inertial acceleration a_i (10^{-1} m s^{-2} , intervals of 0.02 m s^{-2} contoured black), buoyant
 1398 acceleration a_b (10^{-1} m s^{-2} , intervals of 0.02 m s^{-2} contoured cyan), and u - w wind (reference vector
 1399 of 6 m s^{-1} , u wind is relative to the CPLE speed) at (b1) 150 min, (b2) 160 min, and (b3) 170 min;
 1400 (c) equivalent potential temperature θ_e (K, shaded), moisture flux vectors ($q\mathbf{V}$, reference vector of
 1401 $6 \times 10^{-2} \text{ kg m}^{-2} \text{ s}^{-1}$, horizontal component is relative to the CPLE speed), vertical moisture flux (5

1402 $\times 10^{-2} \text{ kg m}^{-2} \text{ s}^{-1}$ contoured black), and cloud water mixing ratio (q_c , 1.2 g kg^{-1} contoured dashed
1403 magenta) at (c1) 150 min, (c2) 160 min, and (c3) 170 min. All the results are averaged relative to
1404 the CPLE (black dashed line) from each time (150 min, 160 min, and 170 min) to 10 min later.
1405 Terrain is shaded gray.

1406

1407

1408

1409

1410

1411

1412

1413

1414

1415

1416

1417

1418

1419

1420

1421

1422

1423

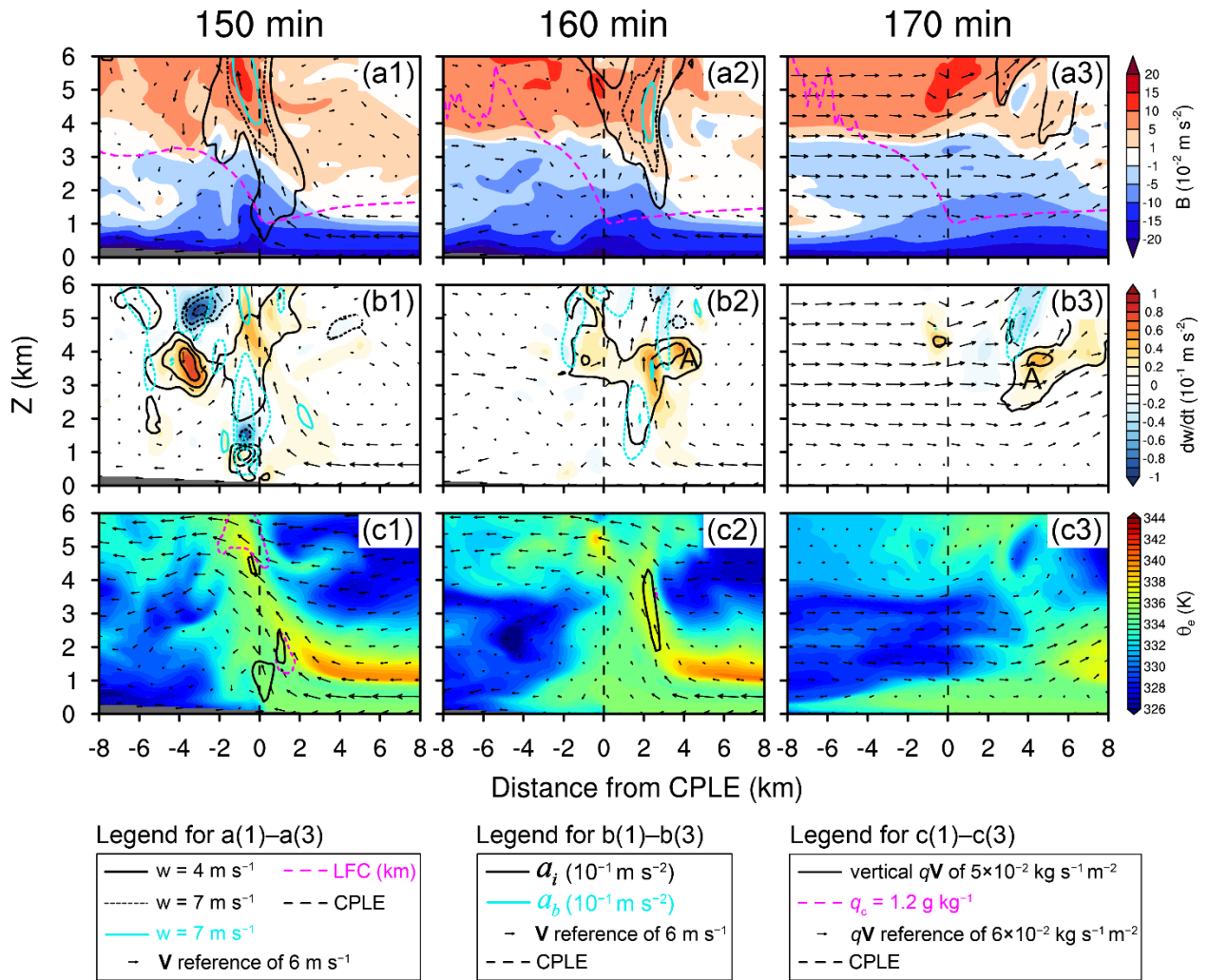


FIG. 15. Same as Fig. 14, but for the experiment with a 1500-m deep, -5-K θ' MABL.

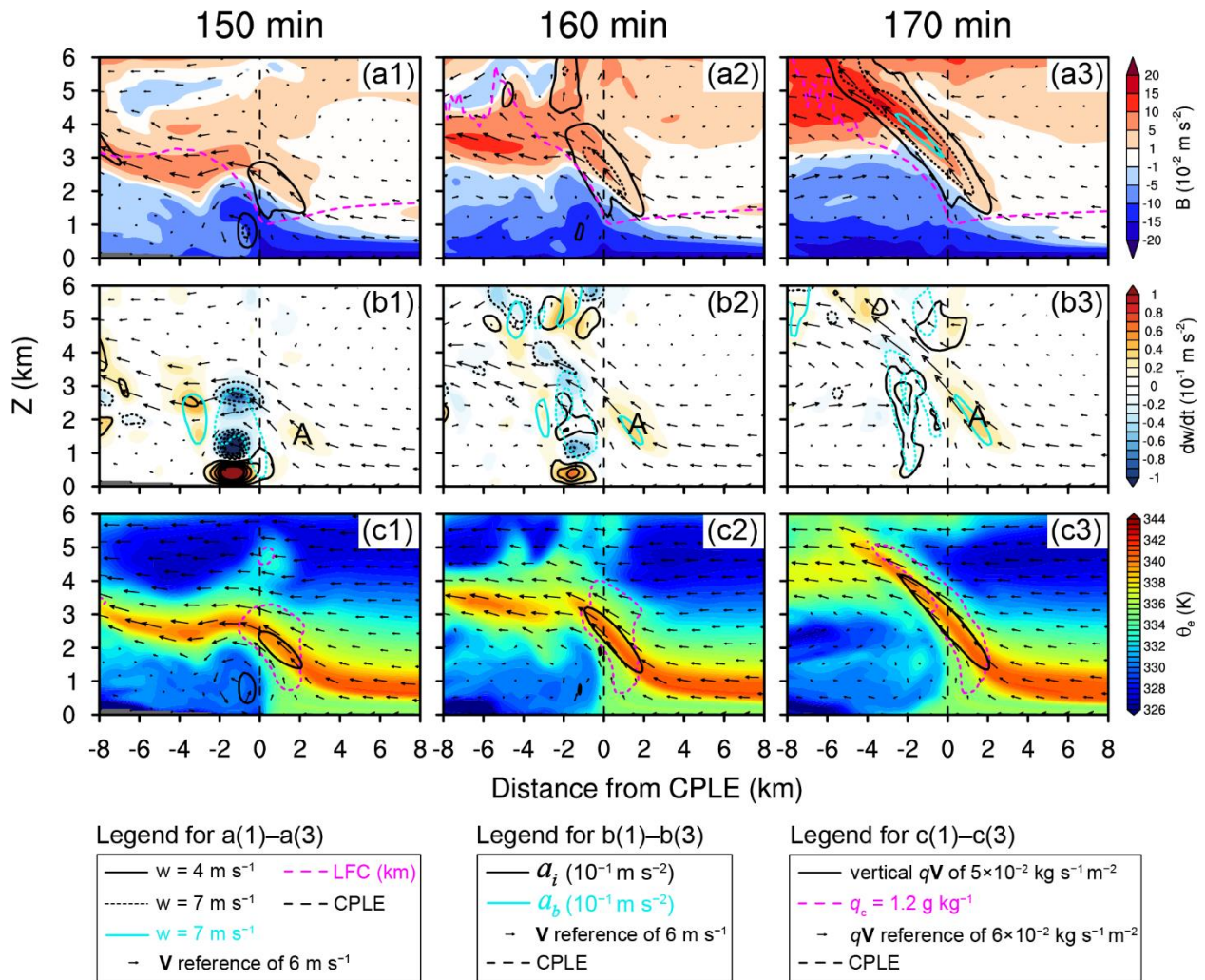
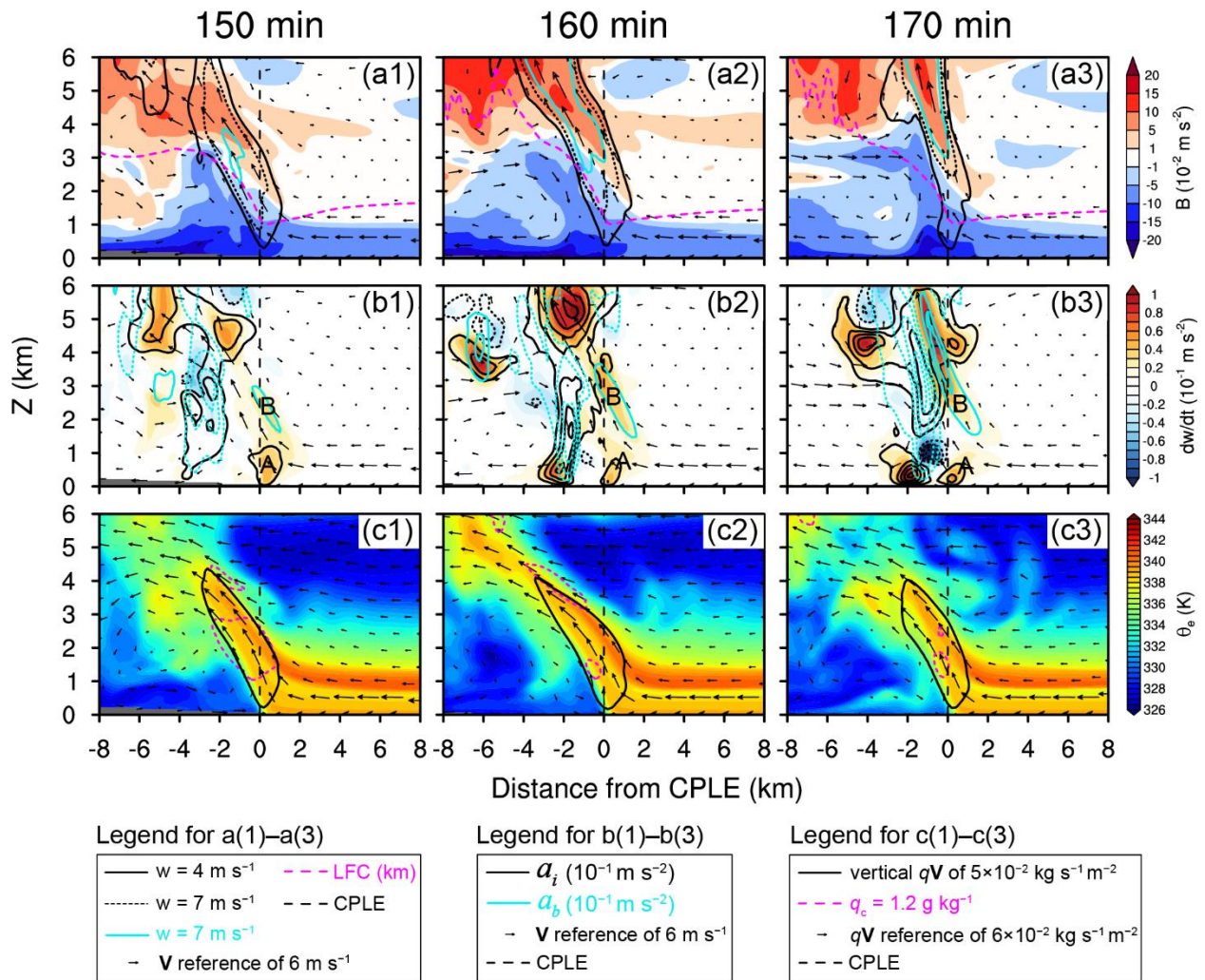


FIG. 16. Same as Fig. 14, but for the experiment with a 500-m deep, $-5\text{-K } \theta'$ MABL.



1432
1433

1434 FIG. 17. Same as Fig. 14, but for the experiment with a 1500-m deep, -3-K θ' MABL.

1435

1436

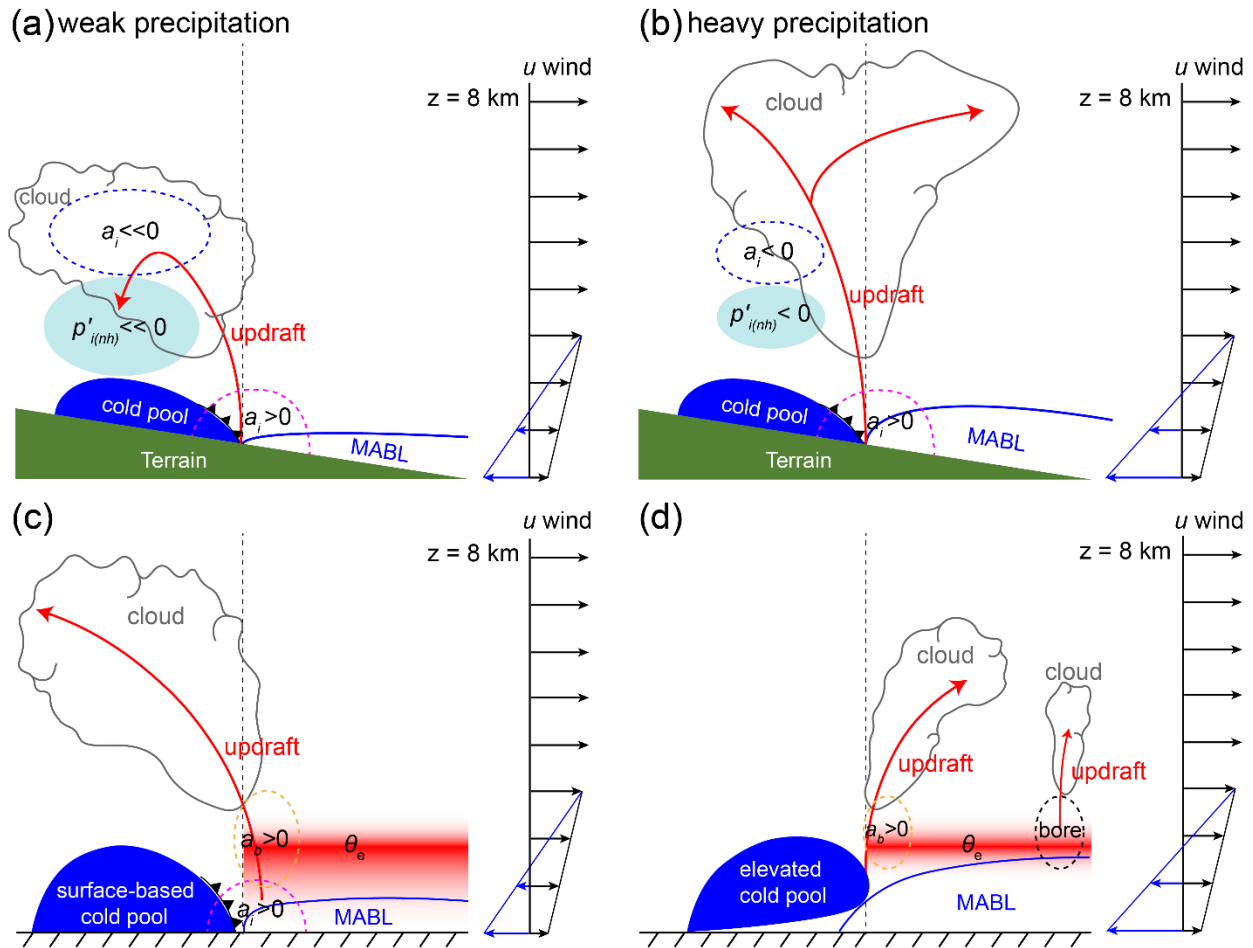
1437

1438

1439

1440

1441



1442

1443

1444

1445

1446

1447

1448

1449

1450

1451

FIG. 18. Schematic diagram of a squall line descending a plateau slope and encountering an upslope moving (a) 500-m deep, $-5\text{-K } \theta'$ MABL, where cold pool lifted air parcels are accelerated downward due to a baroclinically-generated $p'_{i(nh)}$, (b) 1500-m deep, $-5\text{-K } \theta'$ MABL, where cold pool lifted parcels rise unimpeded into the updraft due to the smaller, weaker $p'_{i(nh)}$. Squall lines moving away from the terrain over a (c) 500-m deep, $-3\text{-K } \theta'$ MABL, where a surface-based cold pool lifts low- θ_e air from within the MABL and an elevated bore lifts high- θ_e air from above the MABL into the updraft, (d) 1500-m deep, $-5\text{-K } \theta'$ MABL, where only a thin layer of high- θ_e air is available for bore-induced lift, with no surface-based cold pool ascent.